

國立臺灣大學理學院海洋研究所

碩士論文

Institute of Oceanography

College of Science

National Taiwan University

Master Thesis



使用二相歐拉-拉格朗日模式模擬泥沙在沙
紋上的傳輸

Simulation of Sediment Transport over Ripple
using Two-Phase Euler Lagrange Model

馬丹妮

Danielle L. Manalaysay

指導教授: 曾于恒 博士

Advisor: Yu-Heng Tseng Ph.D.

中華民國 111 年 9 月

September, 2022

國立臺灣大學碩士學位論文
口試委員會審定書
MASTER'S THESIS ACCEPTANCE CERTIFICATE
NATIONAL TAIWAN UNIVERSITY

Simulation of Sediment Transport over Ripples using
Two-phase Euler Lagrange Model

本論文係 馬丹尼 (姓名) R07241107 (學號) 在國立臺灣大學 海洋研究所 (系/所/學位學程) 完成之碩士學位論文，於民國 111 年 9 月 16 日承下列考試委員審查通過及口試及格，特此證明。

The undersigned, appointed by the Institute of Oceanography on 16 (date) 09 (month) 2022 (year) have examined a Master's thesis entitled above presented by Danielle Manalaysay (name) R07241107 (student ID) candidate and hereby certify that it is worthy of acceptance.

口試委員 Oral examination committee:

曾子桓

(指導教授 Advisor)

郭志豪

周逸寧

系主任/所長 Director:

謝志豪



Acknowledgements

“When I meet God, I’m going to ask
him two questions: why relativity?
And why turbulence? I really believe
he’ll have an answer for the first.”

Werner Heisenberg

This study will not be possible without Prof. Tseng’s gracious support, and patience towards me. I am also very grateful to Prof. Chou - thank you for your inputs, guidance, and encouragement on pursuing this topic. I highly appreciate Dr. Kuo as well, for his inputs during my oral defense.

Thank you CODA peeps - Penny, Luna, Vivi, Yichun, Vincent Brian, Sam, and Jenny! Thank you for keeping me sane, translating the documents, and making sure I know the process. I appreciate you all! May we have more milestones to celebrate and cake to eat! Haha. My thesis writing journey in this foreign country have its challenges, but I praise God for my friends back home, who still keep are constant support system - Ate Eunice, Isachar, Ate Crista, Ate Olive, and Ate Lea. I am beyond bless to have you as friends. I am grateful as well to my spiritual family here in Taipei, Every Nation fam thank you so much especially to Jialin, Kevin, Susana, Priscilla, Rona, Teri, Lyn, Richmond, Josm, Maynard John, and so much more who I know prayed and rooted for me.

And of course I will not be here if not for my family, Mama, Papa, Mico and Ate Camille
- I love you! Aica, Erin and Thirdy, can't wait to hug and play with you all again!

I am grateful to this journey 'cause it brought me close to God, I saw and experience
how amazing He is. I am excited to do more science and see how our can our limited
capacity can capture the beauty and mysteries of His immense complex creation. May I
always be humble and be in awe of His Glory. To Him be the all the praise!





Abstract

Ripple indicators remain to be a major limitation of large-scale hydrodynamic modelling in coastal environments due to the lack of appropriate validation and direct measurement of near-bed dynamics. This limitation can be overcome with improved small-scale process models that can capture fluid-particle interactions and near-bed dynamics over the ripples. Here, we simulate the sediment transport over ripples induced by an oscillatory flow using a two-phase Euler-Lagrange model. The vortex ripple dimension, oscillatory flow condition, and sediment grain information are obtained from a wave-tunnel laboratory experiment. The two-phase model can well simulate the key patterns of observed oscillatory velocity flow field over a vortex ripple. Particularly, the weaker vortex can be found on the stoss side as compared to the stronger vortex on the lee side during reversals of the oscillatory flow that were ahead of the free-stream velocity. Sensitivity tests of three different sediment grain diameters (0.35mm, 0.44mm and 0.53 mm) are compared to examine the feedback of sediments particles with varying grain sizes. Our simulation

results showed that finer sediment particles (0.35 mm and 0.44 mm) have higher particle motion and entrainment that enhanced the local vortex formation but neither high enough to alter the oscillatory flow nor enhance the turbulent kinetic energy. On the other hand, coarser sediment (0.53 mm) have lesser particle motion and entrainment but induced constant inter-phase drag that increasingly enhanced the turbulent kinetic energy of the oscillatory flow. Our results showed that different sediment grain size could have different drag contribution to the energy budget of an oscillatory flow.

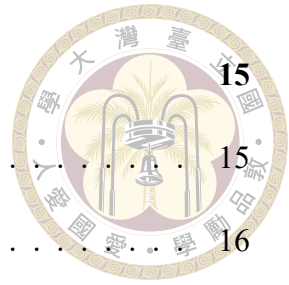
Keywords: ripple, oscillatory flow, particles, sediment transport, numerical simulation



Contents

	Page
Acknowledgements	ii
Abstract	iv
Contents	vi
List of Figures	viii
List of Tables	xi
Chapter 1 Introduction	1
1.1 Coastal Sediment Transport	1
1.2 Ripples and Small Scale Sediment Transport Studies	2
1.3 Objective of Our Study	3
Chapter 2 Methodology	5
2.1 Two-phase Euler-Lagrange Model	5
2.2 Numerical Scheme	7
2.3 Simulation Setup	7
2.3.1 Ripple Laboratory Experiment: Mr5b63	7
2.3.2 Flow Settings	8
2.3.3 Spatial and Temporal Settings	9
2.3.4 Experiment Cases	9

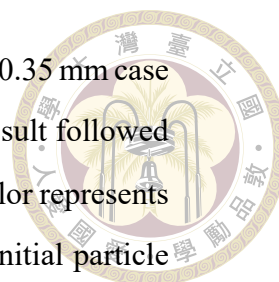
Chapter 3	Results	15
3.1	Validation	15
3.2	Time Dependent Results	16
3.2.1	Control Case: Flow Velocity	16
3.2.2	Case with Sediments: Instantaneous Sediments distribution	17
3.2.3	Case with Sediments: Span-wise Summation of Sediments Distribution	18
3.2.4	Case with Sediments: Flow Field Difference	18
3.3	Time-Averaged Results	19
Chapter 4	Discussion	41
Chapter 5	Summary	47
References		49





List of Figures

2.1	Positive values $\mathbf{u}(t)$ correspond to onshore flow while negative values of $\mathbf{u}(t)$ correspond to offshore directed	11
2.2	Ripple width $\lambda = 0.41$ m and ripple height $\eta = 0.076$ m	11
2.3	$Lx \times Ly \times Lz = 1.64$ m \times 0.6 m \times 0.41 m	12
2.4	Sediments particles were initialized between $x = 0.5$ and 0.9	12
3.1	Time series of spanwise-average wall stress in the stream-wise direction. After one period the simulation reached quasi-steady solution.	22
3.2	Snapshot of the instantaneous span-wise averaged vorticity on the first cycle. The formation of the vortex started at the lee slope at the end of the onshore flow $t = 0.48T$ and the ejection to the crest happened flow reversal $t = 0.52 T$	22
3.3	Flow field results of Mr5b63 laboratory experiment: Screenshot of Figure 1 on van der Werf et al. (2007). Top most panel is the calculated free-stream velocity, the letters corresponds to the t/T where following oscillatory velocity - flow feature occurs: (A) off-onshore flow reversal; (B) free stream is accelerating onshore; (C) maximum onshore free-stream velocity; (D) onshore free-stream velocity deceleration; (E) on-offshore flow reversal; (F) free stream acceleration offshore; (G) maximum offshore free stream velocity; and (H) offshore free-stream velocity deceleration. . . .	23
3.4	Top most panel is the calculated free-stream velocity with the letters (A) to (H) that corresponds to the approximate time of 8 flow features described in Figure3.3. Panels (A) to (H) are the flow field results of the control case (no sediment) simulations.	24



3.5 All panels are the top view of the particle volume fraction for 0.35 mm case at five instances: at $t/T = 0.02, 1, 2, 3,$ and 4 - the initial result followed by the results at end of every oscillatory flow period. The color represents the logarithmic particle volume fraction normalize by the initial particle volume value. The initial value is at $t/T = 0.02,$ is almost to zero as values are close to the initial particle volume value. The lighter shade means the particle volume fraction is lower from the initial value, the darker shade means the particle volume fraction is higher from from initial value. 25

3.6 Same as Figure 3.5 but for 0.44 mm case. 26

3.7 Same as 3.5 but for 0.53 mm case. 27

3.8 Top most panel is the calculated free-stream velocity with the letters (A) to (H) that corresponds to the $\approx t/T$ of 8 flow features described in Figure 3.3. Panels (A) to (H) are the span-wise total particle volume fraction for all cases. Red marker represents the 0.35 mm case, blue marker represents the 0.44 mm case and green marker represents the 0.53 case. 28

3.9 Continued. 29

3.10 Top most panel is the calculated free-stream velocity with the letters (A) to (H) that corresponds to the $\approx t/T$ of 8 flow features described in Figure 3.3. Panels (A) to (H) are the flow field difference results between the 0.35 mm case and control case (no sediment) simulations. The color represent the magnitude overlaid with the corresponding velocity vectors. 30

3.10 Continued. 31

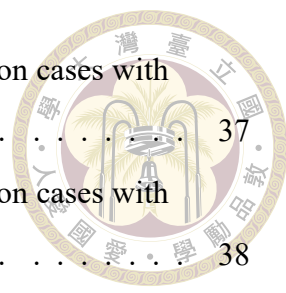
3.11 Same as Figure 3.10 but for 0.42 mm case. 32

3.11 Continued. 33

3.12 Same as Figure 3.10 but for 0.53 mm case. 34

3.12 Continued. 35

3.12 Period- and spanwise- mean velocity flow field based on Mr5b63 experiment of van der Werf et al. (2007): Screenshot of Figure A1 on van der Werf et al. (2008). 36



3.12	Top-most panel is the control case followed by the simulation cases with sediments - 0.35 mm case, 0.44 mm case and 0.53 mm case.	37
3.12	Top-most panel is the control case followed by the simulation cases with sediments - 0.35 mm case, 0.44 mm case and 0.53 mm case.	38
3.12	Top-most panel is the control case followed by the simulation cases with sediments - 0.35 mm case, 0.44 mm case and 0.53 mm case.	39
4.1	Top panel is the time series of the total kinetic energy for control case. Middle panel is the time series of the total kinetic energy for the simulation case with sediments. Note that there are three lines plotted on this panel. Last panel is the difference of the second and first panel. Black-filled marker is for 0.35 mm case, gray-filled marker is for 0.44 mm case and white-filled marker is for 0.53 mm case.	44
4.2	Time series turbulent kinetic energy for all three cases. Black-filled marker is for 0.35 mm case, grey-filled marker is for 0.44 mm case and white-filled marker is for 0.53 mm case.	45
4.3	Time series ΔPE due to the motion of sediment particles for all three cases. Black-filled marker is for 0.35 mm case, grey-filled marker is for 0.44 mm case and white-filled marker is for 0.53 mm case.	45
4.4	Time series of energy dissipation due to inter-phase drag for all three cases. Black-filled marker is for 0.35 mm case, gray-filled marker is for 0.44 mm case and white-filled marker is for 0.53 mm case	46



List of Tables

2.1 Overview of all 4 experiment cases: Sediment diameter size \mathbf{d}_{sed} , Relaxation time τ_{sed} , Number of particles per grid \mathbf{N}_{grid} , Total number of particle \mathbf{N}_{sed} , Total simulation time $\mathbf{CPU}_{\text{time}}$ 13

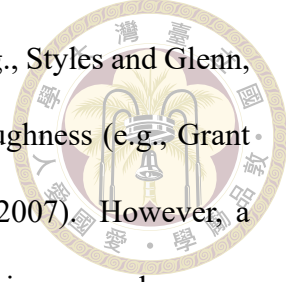


Chapter 1 Introduction

1.1 Coastal Sediment Transport

There has been an increasing man-made offshore activity world wide, including Taiwan. With its goal of achieving sustainable renewable energy, the Taiwan government has leased an area in Greater Chunghua on the western side of the country for offshore wind farm development. As offshore wind farm developers come to the country, one of the vital concern is the present sea bed condition and how will it be affected during the extreme condition, such as typhoons which occur commonly in the western North Pacific. Several vital concerns such the seabed current condition and seabed projection on extreme event has to be addressed.

To answer these concerns, geomorphological solutions such as coastal sediment transport modeling could be performed. However, coastal sediment transport modeling is still intrinsically empirical as involves complex sub-grid processes, such as near-bed hydrodynamics and turbulent sediment particle interaction, that are not yet well understood or fully resolved (Amoudry and Souza, 2011). These processes are then carefully parameterized on the bottom boundary layer (BBL), usually in $O(10\text{m})$ of thick, of coastal hydrodynamic models. The BBL formulation is important as it determines the bottom stress used in sediment transport rates. The formulation can be either simple drag-coefficient routines or

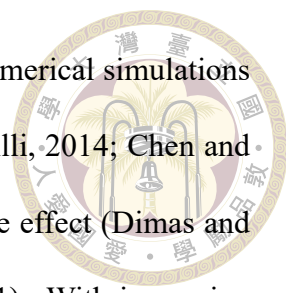


more complex routines that accounts the wave-current interaction (e.g., Styles and Glenn, 2000; Mellor, 2002; Soulsby and Damgaard, 2005) and bedform roughness (e.g., Grant and Madsen, 1982; Nielsen, 1986; Li and Amos, 2001; Van Rijn, 2007). However, a study by Warner et al. (2008) points out that although the differences in approach among the more complex BBL routines are small, they can produce significantly different results. Likewise, there is precaution on using constant roughness indicator as it could overestimate sediment-transport values and is only recommended for preliminary baseline studies (Brakenhoff et al., 2020). Thus, although regional ocean models have included a great deal of detail to describe sediment transport, there is still a need to further pursue studies of sediment grain size effect on both numerical and experimental, to achieve a better parameterization and accuracy.

1.2 Ripples and Small Scale Sediment Transport Studies

When bedforms are present, additional drag constitutes to the bottom stress that affects hydrodynamics and sediment transport (Van Rijn, 2007; Cherlet et al., 2007). Ripples are one of the common bedforms in coastal environment, formed by interaction of non-cohesive sediment particles with either unidirectional currents (Richards, 1980) or by the wave-driven oscillatory flow (Blondeaux, 1990). Ripples are characterized by ripple width, λ , of $O(0.1)$ and ripple height, η , $O(0.01)$ and are ubiquitous in coastal environment even in Taiwan (Liao and Yu, 2005; Liao et al., 2008; Zhou et al., 2018).

Direct observation of ripples on field is still difficult that is why efforts have been poured in to large-scale laboratory experiments to carry out ripples in par on what is on field - such as by O'Donoghue et al. (2006), van der Werf et al. (2007), and Yuan and

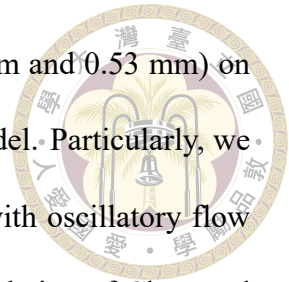


Wang (2019). These detailed measurements were used to validate numerical simulations of sediment transport (e.g., van der Werf et al., 2008; Harris and Grilli, 2014; Chen and Yu, 2015), particle interaction (Finn et al., 2016), sediment grain size effect (Dimas and Leftheriotis, 2019), and sand migration (Salimi-Tarazouj et al., 2021). With increasing computation power over the recent years, Finn et al. (2016) were able to carry out two-phase point-particle model to simulate the near-bed particle-particle interaction on a vortex ripple with high fidelity. Particularly, their results showed near-bed oscillatory flow in ripples are effective in sorting and segregating particle size, with coarser particles resting above the finer particles. Therefore, there is low particle motion with the coarse particles on the surface of the ripple, while the finer particle have an armouring mechanism that impedes vertical particle motion, and thus only during the highest energetic phase of oscillatory flow can suspend substantial amount of particles. However, the authors pointed out that the unrealistic soft restitution coefficients adopted to account particle collision on their model may lead to underestimation of energy induced by larger particles. Thus, further studies are needed to investigate how large particles may contribute to the energy of an oscillatory flow that can be applied to coastal environments as fully resolved information on such large particle regime are still limited on solid-gas systems (e.g., Tenneti et al., 2011; Tang et al., 2014).

1.3 Objective of Our Study

To have a better understanding of how the sediment grain size and bedform affect turbulent oscillatory flow, we extended the numerical study of Chou and Shao (2016) in investigating the particle size drag contribution to the energy budget by considering larger particles and different flow scenario compared to their experiment setup. Our objective

is to compare effect of different larger grain sizes (0.35 mm, 0.44 mm and 0.53 mm) on an oscillatory flow over ripple from a two-phase Euler-Lagrange model. Particularly, we present the simulation results of the sediment particles interacting with oscillatory flow field over space and time. Finally, adopting the energy budget calculation of Chou and Shao (2016), we discuss how the different grain sizes could have different particle motion and interphase drag that could contribute to the turbulent kinetic energy of the oscillatory flow.





Chapter 2 Methodology

2.1 Two-phase Euler-Lagrange Model

The two-phase Euler-Lagrange model used in this study was developed by Chou et al. (2015). The momentum equation of a sediment solid particle is as follows,

$$m_{sed} \frac{d\mathbf{u}_{sed}}{dt} = m_{sed} \frac{|\mathbf{u}_{cont|sed} - \mathbf{u}_{sed}|}{\tau_{sed}} + (m_{sed} - m_{flo})\mathbf{g} \quad (2.1)$$

where m is the mass, with subscripts sed and flo , for the sediment phase and fluid phase respectively, \mathbf{u}_{sed} , is the velocity of the sediment particle, $\mathbf{u}_{cont|sed}$ is the velocity of the continuum phase evaluated at the location of the sediment particle, and \mathbf{g} is the gravitational acceleration. The sediment relaxation time, τ_{sed} , can be obtained by, Schiller and Naumann (1935)

$$\tau_{sed} = s \frac{D_{sed}^2}{18\nu} (1 + 15Re^{0.687})^{-1}, \quad (2.2)$$

in which $s = \rho / \rho_o$ is the density ratio of sediment and fluid phases, D_{sed} is the sediment diameter, ν is the kinematic viscosity, and Re is the sediment Reynolds number,

$$Re = \frac{|\mathbf{u}_{cont|sed} - \mathbf{u}_{sed}| D_{sed}}{\nu} \leq 800. \quad (2.3)$$

On the other hand, the momentum equation for the continuous fluid phase is described as

$$\frac{\partial \mathbf{u}}{\partial t} + \mathbf{u} \cdot \nabla \mathbf{u} = -\frac{1}{\rho_o} \nabla P + \nu \nabla^2 \mathbf{u} + \mathbf{f} \quad (2.4)$$



where \mathbf{u} is the three dimensional velocity field of the fluid phase and P is the hydrodynamic pressure. The forcing term, \mathbf{f} , is the total sediment drag acting on the fluid,

$$\mathbf{f} = -s \sum_{m=1}^{N_{sed}} \phi_{sed} \frac{|\mathbf{u}_{|sed,m} - \mathbf{u}_{sed,m}|}{\tau_{sed,m}} \quad (2.5)$$

where N_{sed} is the total number of particles in the control volume, and ϕ_{sed} is the volume fraction of a single sediment.

In this study, we assume the sediments have zero inertia, wherein the sediment drag is in equilibrium with the gravitational force, giving sediment velocity,

$$\mathbf{u}_{sed} = \mathbf{u}_{cont|sed} + \tau_{sed} \mathbf{g}' = \mathbf{u}_{cont|sed} - w_s \hat{\mathbf{e}}_3, \quad (2.6)$$

where $\hat{\mathbf{e}}_3$ is the unit in the vertical direction, $\mathbf{g}' = (1 - 1/s)\mathbf{g}$ is the reduced gravity for a single sediment, and w_s is the settling speed. With this assumption, the sediment forcing on Eq.2.5 can be written, in equilibrium, as

$$\mathbf{f}_{eq} = sN_{sed}\phi_{sed}\mathbf{g}' = s\phi_{sed}\mathbf{g}' \quad (2.7)$$

Thus, the momentum equation for continuous fluid in equilibrium is

$$\frac{\partial \mathbf{u}}{\partial t} + \mathbf{u} \cdot \nabla \mathbf{u} = -\frac{1}{\rho_o} \nabla P + \nu \nabla^2 \mathbf{u}_c + s\phi_{sed}\mathbf{g}', \quad (2.8)$$

The buoyant force is equal to the feedback force of the particles equilibrium to the fluid

phase.



2.2 Numerical Scheme

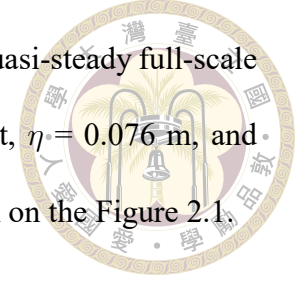
The two-phase Euler-Lagrange model is coupled with a particle moving algorithm in this study based on the Computational Fluid Dynamics (CFD) code originally developed by Zang (1994). All spatial derivatives except convective terms are discretized with second-order central differences; the convective terms, on the other hand, are discretized using QUICK. For time advancement, Crank – Nicholson is used for the diagonal viscous term, while the 2nd order Runge-Kutta method is used for all others. The momentum equation is advanced such that the calculated divergence-free velocity field each time step is corrected by the predicted velocity with the pressure gradient based on a fraction-step method. Parallelization is achieved via message parsing interface by Cui (1999). The present numerical model has been applied to study the particle-induced Rayleigh-Taylor instability, double-diffusive sedimentation and point-force representation for fine suspended particles ((Chou et al., 2015; Chou and Shao, 2016)).

2.3 Simulation Setup

2.3.1 Ripple Laboratory Experiment: Mr5b63

The ripple dimension, flow conditions and sediment particle information considered in this study are obtained from the measurement of the ‘Mr5b63’ controlled-experiment performed by van der Werf et al. (2007). The facility used for the experiment is a closed-loop piston-driven oscillatory flow tunnel which includes provided phase resolved fluid

flow and sediment concentration observation results. The resulting quasi-steady full-scale ripple dimension from the 'Mr5b63' experiment has a ripple height, $\eta = 0.076$ m, and ripple length, $\lambda = 0.41$ m, thus gives ripple ratio, $\eta/\lambda = 0.19$, as shown on the Figure 2.1,



2.3.2 Flow Settings

The oscillatory fluid velocity $\mathbf{u}(t)$ implemented in our study is from the following expression,

$$\mathbf{u}(t) = \mathbf{u}_1 \omega \cos(\omega t - \gamma) + \mathbf{u}_2 \omega \cos(2\omega t - 2\gamma) \quad (2.9)$$

where \mathbf{u}_1 and \mathbf{u}_2 , are the first and second harmonic flow velocity amplitudes (0.54 m/s and 0.09 m/s, respectively), $\omega = 2\pi/T$ is the angular velocity, $T = 5$ s is the flow period. The phase shift γ is included to satisfy $\mathbf{u}(0) = 0$,

$$\gamma = \cos^{-1}\left(\frac{\sqrt{\mathbf{u}_1^2 + 8\mathbf{u}_2^2} - \mathbf{u}_1}{4\mathbf{u}_2}\right) \quad (2.10)$$

The flow velocity $\mathbf{u}(t)$ is shown in Figure 2.1, \mathbf{u}_1 and \mathbf{u}_2 were set so that the maximum velocity $\mathbf{u}_{max} \approx 0.63$ m/s. The velocity asymmetry $R = (\mathbf{u}_1 + \mathbf{u}_2)/2\mathbf{u}_1 \approx 0.6$, with maximum onshore velocity is achieved at $t/T \approx 0.22$, while maximum offshore velocity is achieved at $t/T \approx 0.72$. The flow reversal occurs $t/T \approx 0.48$. The root-mean-square orbital velocity, $\mathbf{u}_{rms} = \sqrt{0.5\mathbf{u}_1^2 + 0.5\mathbf{u}_2^2}$ provides orbital amplitude, $a_o = \sqrt{2}\mathbf{u}_{rms} \approx 0.44$ m/s. Positive values of $\mathbf{u}(t)$ corresponds to 'onshore' flow and negative values to 'offshore' flow. With generalized coordinate system used in the EL model, the boundaries on the streamwise (x) and spanwise (z) directions are periodic, while the bottom boundary (y) have a no-slip condition.



2.3.3 Spatial and Temporal Settings

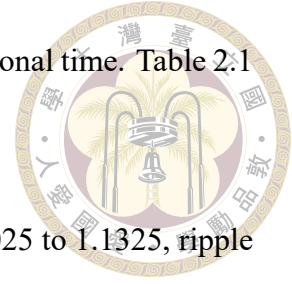
The domain length, L_x , is set to $4\lambda = 1.64\text{m}$, to avoid the effect of the periodicity near the boundary; the domain width, L_z , is set to $\lambda = 0.41\text{m}$ and the domain height, L_y , is set to $\approx 8.3\eta = 0.6\text{m}$. Grid size $N_i \times N_j \times N_k = 960 \times 192 \times 240$, corresponds to resolution $\Delta x = \Delta z = 1.7 \times 10^{-3}\text{mm}$. The vertical resolution is $0.0011\text{mm} \leq \Delta y \leq 0.0074\text{mm}$ due to the stretching ratio $\Delta y_{k+1}/\Delta y_k = 1.01$. Total core processors used for simulation is 1200, due to following the grid decomposition: $p_x \times p_y \times p_z = 20 \times 15 \times 5$.

All simulation was ran for 8 flow periods with a time step of $\Delta t = 4 \times 10^{-4}\text{s}$ when sediment particles are not present. Otherwise the time step, $\Delta t = 5 \times 10^{-5}\text{s}$ when sediment particles are present. The details of the simulated experiment cases are discussed in the next section.

2.3.4 Experiment Cases

There are 4 experiment cases presented in this study: control (no sediment), 0.35 mm, 0.44 mm and 0.53 mm. The control case is served as the baseline simulation to compare with the other three sensitivity cases. Sediment particles are initiated after the fourth oscillatory period. Three different sediment particles (diameters: 0.35 mm, 0.44 mm and 0.53 mm) are introduced at the bottom-most grid $N_j = 1$, at $z = 0.15\text{m} - 0.25\text{m}$, $x = 0.5 - 0.9\text{m}$ (Figure 2.4). Same particle volume fraction per grid is initialized for these simulation cases. In such condition, the 0.35 mm case has greatest number of particles per grid, $N_{grid} = 143$, corresponding total number of particles $N_{sed} = 1,940,796$. The 0.44 mm case has $N_{grid} = 72$, thus corresponding to total of number of sediments of $N_{sed} = 977,184$. The 0.53 mm case has $N_{grid} = 41$, thus corresponding total of number of sediments of N_{sed}

= 556,452. Including more particles per grid requires more computational time. Table 2.1 summarizes the setup of these experiment cases.



The results of the simulation presented here is from $x(m) = 0.3025$ to 1.1325 , ripple width long. The horizontal x-axis is normalized by the ripple length and vertical y-axis is normalized by ripple height. All of the flow field results are span-wise-average over the z-axis over the last oscillatory period of the simulation, unless otherwise mentioned.

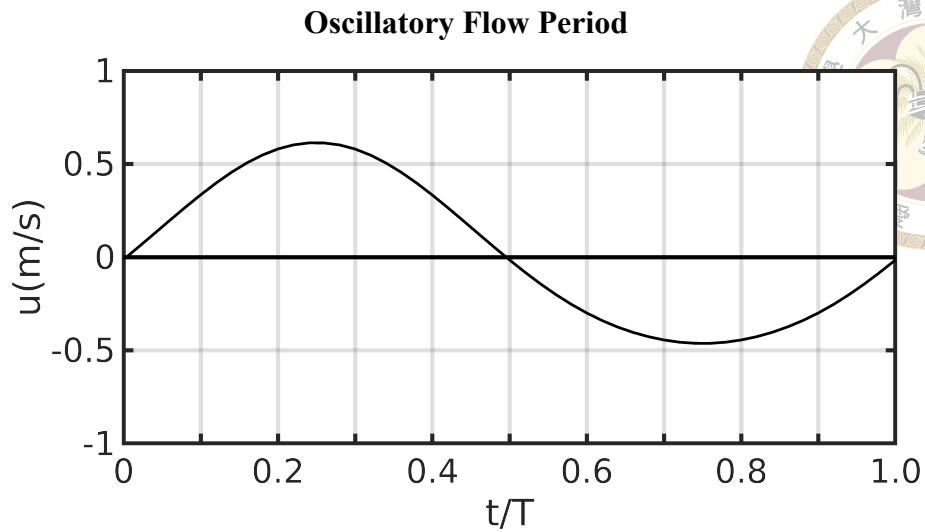


Figure 2.1: Positive values $u(t)$ correspond to onshore flow while negative values of $u(t)$ correspond to offshore directed

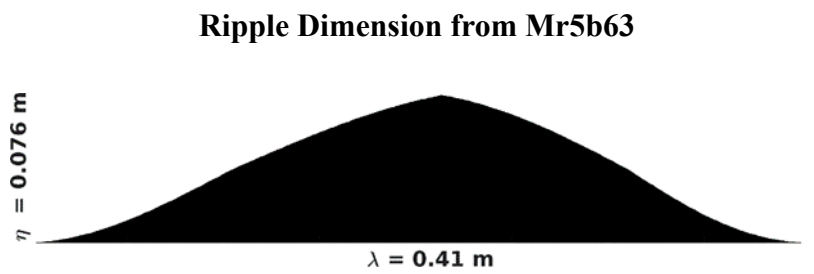


Figure 2.2: Ripple width $\lambda = 0.41 \text{ m}$ and ripple height $\eta = 0.076 \text{ m}$



Simulation Domain

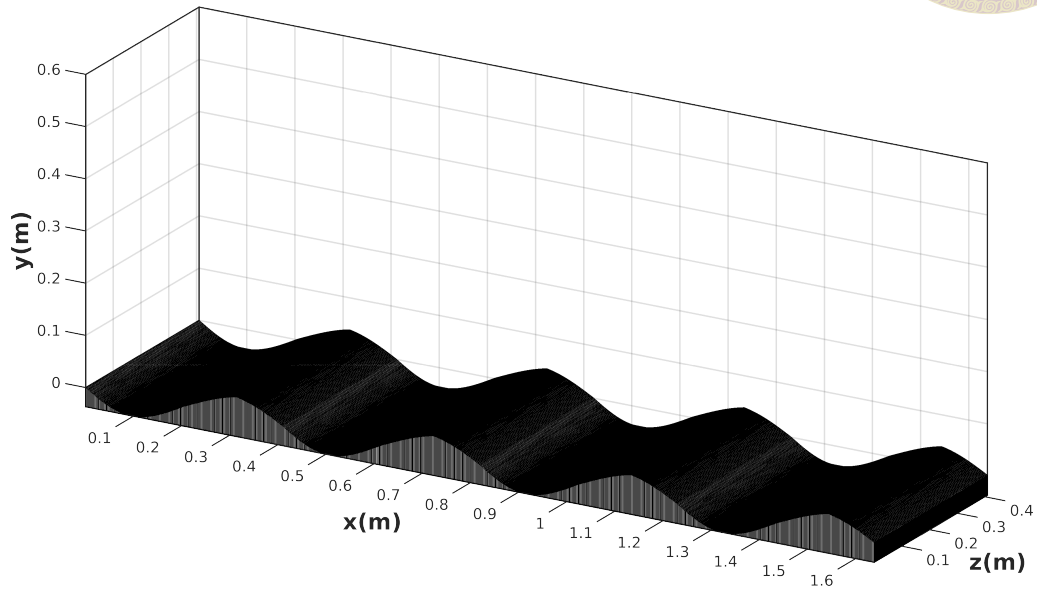


Figure 2.3: $L_x \times L_y \times L_z = 1.64 \text{ m} \times 0.6 \text{ m} \times 0.41 \text{ m}$

Sediment Initialization

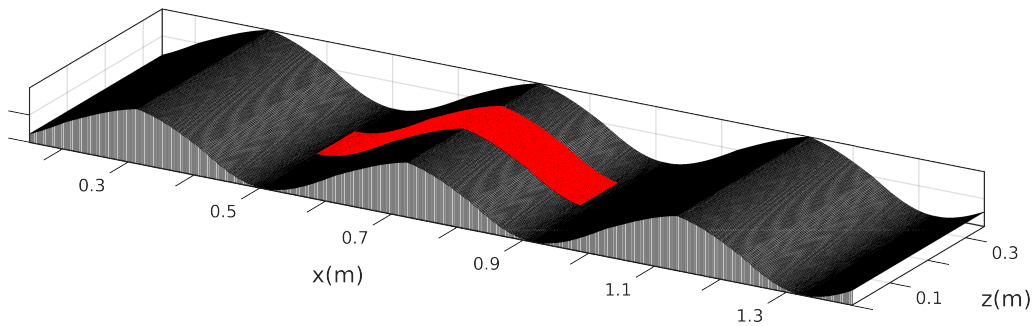


Figure 2.4: Sediments particles were initialized between $x=0.5$ and 0.9

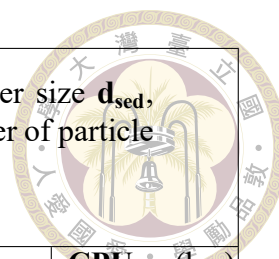


Table 2.1: Overview of all 4 experiment cases: Sediment diameter size d_{sed} , Relaxation time τ_{sed} , Number of particles per grid N_{grid} , Total number of particle N_{sed} , Total simulation time CPU_{time}

Case	d_{sed} (mm)	τ_{sed} (s)	N_{grid}	N_{sed}	CPU_{time} (hrs)
Control	n/a	n/a	n/a	n/a	18.25
0.35 mm	0.35	0.018	143	1,940,796	140.31
0.44 mm	0.44	0.029	72	977,184	96.18
0.53 mm	0.53	0.041	41	556,452	57.77



Chapter 3 Results

3.1 Validation

The baseline simulation achieved a quasi-steady periodic solution quickly after the first oscillatory cycle, as seen in the spatially averaged wall-shear stress, τ_b

$$\tau_b = -\mu \frac{\partial U}{\partial y} \quad (3.1)$$

The time series of the computed spatially averaged wall shear stress in the stream-wise direction of the base case simulation is shown in Figure 3.1. The known vortex formation–ejection process, reported various studies (e.g., Sleath, 1982; Blondeaux and Vittori, 1991; Zedler et al., 2006; Chen and Yu, 2015; Salimi-Tarazouj et al., 2021) is captured by our simulation as shown in Figure 3.2. The vortex is formed due to flow separation at the ripple crest during the maximum offshore flow, that grows into the lee side during the onshore deceleration ($t = 0.48 T$) and its ejection during flow reversal ($t = 0.52 T$).

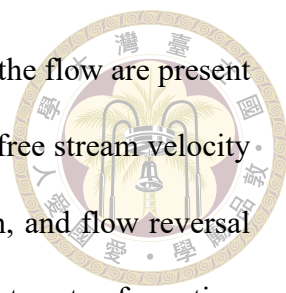


3.2 Time Dependent Results

3.2.1 Control Case: Flow Velocity

The time dependent flow velocity from the control experiment (Figure 3.4) showed good agreement with the experiment (Figure 3.3). In these figures, eight key flow patterns are shown, representing the different flow states within a cycle : (A) off-onshore flow reversal; (B) free stream is accelerating onshore; (C) maximum onshore free stream velocity; (D) onshore free stream velocity deceleration; (E) on-offshore flow reversal; (F) free stream acceleration offshore; (G) maximum offshore free stream velocity; and (H) offshore free-stream velocity deceleration.

Overall the simulated results in this study were in good comparison to the general velocity flow patterns. However there is a lag in the temporal flow reversals as compared to the measured results which was observed on other simulation work (Finn et al. (2016)). Even without the sediment particle the simulated velocity flow was able to capture the weaker vortex on the stoss side during off-onshore flow reversal (A) as compared to the stronger vortex on the lee side during the on-offshore flow reversal (E). However, during flow reversals (A and E), the free stream velocity, above $y/\eta \geq 1$ is not completely zero as compared to the measured results. During the acceleration of free stream velocity onshore (B) and offshore (F) have high jet flow over the crest that extends towards the ripple trough due to the coherent ejection of the stoss - and lee - side vortices is weaker with the absence of sediment particles in the base case simulation. Likewise, deceleration of velocities towards the slope direction during acceleration of flow-phase (B and F), rather the flow constant from free stream until the bed. During the maximum free stream onshore (C) and



offshore (G), flow separation near the ripple flank in the direction of the flow are present in the simulation but not as high in the measured results. At time of free stream velocity deceleration (D and H), high velocity in the crest are no longer seen, and flow reversal happened at the ripple surface in the [lee , stoss] formed into a distinct vortex formation. The height of flow separation during the onshore free stream velocity deceleration (D) reaches up to $\approx 0.5y/\eta$ while the offshore free stream velocity deceleration (H) reaches to $\approx 0.2y/\eta$ only.

3.2.2 Case with Sediments: Instantaneous Sediments distribution

Here we present in Figure 3.5 to Figure 3.7, the time-dependent result on simulation cases with sediment particles introduced on the same condition as the control case described above. The top most panel for all the figures is the instantaneous plot after the initialization at ($t/T = 0.02$) while the succeeding plots are the instantaneous plots at the end of each oscillatory flow period. Regardless of the flow direction, for 0.35 mm and 0.44 mm cases - finer sediments with smaller particle relaxation time - the particle moved down the ripple slopes with the high accumulation at ripple trough $x/\lambda = \pm 0.5$. At the end of the simulation at $t/T = 4$, of the 0.35 mm and 0.44 mm case shown Figure 3.5 and Figure 3.5 respectively, we can see the sediment accumulation at the ripple trough expanding up to $z/\eta = \pm 0.25$. However for 0.53 mm case - coarser sediments with larger particle relaxation time, the motion is rather slow. Figure 3.7 shows at the end of each oscillatory period the particle volume fraction have an the same distribution as $t/T = 2$, indication of no significant particle motion.

3.2.3 Case with Sediments: Span-wise Summation of Sediments Distribution



To give more insight on the sediment particle motion during an oscillatory flow, Figure 3.9 shows the span-wise total particle volume fraction for all the cases on the last oscillatory period. Consistent with the previous section the 0.35 mm and 0.44 mm cases have low volume fraction at the vortex ripple where the sediment particles were initialized as it moved down the slope and accumulated at the ripple troughs. Although the general trend of the motion particles are moving down the slope, there are some sediment particles entrained that followed the oscillatory flow. There are sediment going onshore, on to the right flank of the the adjacent vortex ripple $x/\lambda > 0.5$, as seen on Figure 3.9 A to D. Likewise there are sediments going offshore, on to the left flank of the adjacent vortex ripple, $x/\lambda = < -0.5$ as seen on Figure 3.9 E to F. On the other hand 0.53 mm case seem undisturbed by the flow, maintaining the value of throughout the oscillatory period.

3.2.4 Case with Sediments: Flow Field Difference

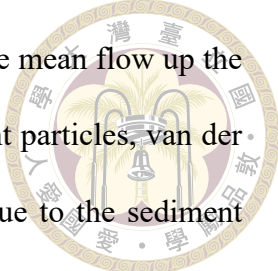
How does the this affect the oscillatory flow? The time-dependent feedback of the sediment presence to the oscillatory flow is shown Figure 3.10 to Figure 3.12. These figures show the flow field difference of cases with the sediments and control case during the last flow period. For 0.35 mm and 0.44 mm cases the sediment behavior is similar, thus the effect on the flow is similar as well, and the details are as follow: During the (A) offshore flow reversal, , there is circulation cell formed at stoss slope $x/\lambda = -0.25$, going onshore to the ripple crest as the onshore flow accelerates (B). This circulation cell is no longer seen at the maximum onshore flow (C) for both cases. During onshore free stream

velocity deceleration (D) there is stronger circulation cell being formed at the ripple trough that is continuously seen during on-offshore flow reversal and (F) free stream acceleration offshore. This circulation cell is washed away during the (G) maximum offshore free stream velocity; and (H) offshore free-stream velocity deceleration.

For the 0.53 mm case, since the sediment particles are closely packed through out the oscillatory flow, it affected the flow more as seen on Figure 3.12. During the (A) offshore flow reversal, there is an offshore flow on the lee slope surface of the adjacent vortex ripple on the left up to $x/\lambda = -0.75$ and onshore flow up to the crest of adjacent vortex ripple on the right up $x/\lambda = 1$. These offshore and onshore flow on the ripple surface continues to move to the right as the (B) free stream is accelerating onshore and seen mostly on the stoss slopes during the (C) maximum onshore free stream velocity. During the (D) onshore free stream velocity deceleration the formation of the circulation cell on the ripple trough and ejected over the lee slope during (E) on-offshore flow reversal and (F) free stream acceleration offshore, but there is still a continues onshore flow on the lee slope and offshore flow on the stoss slope. During the (G) maximum offshore free stream velocity there is an onshore flow on the $x/\lambda > 0$ the surface. This onshore flow increased in height up to $y/\eta = 0.5$ during (H) offshore free-stream velocity deceleration.

3.3 Time-Averaged Results

Figure 3.12 shows the period- mean flow velocities over the last oscillatory, where the mean free stream velocity is onshore directed but, at a ripple length above the crest at $y/\eta = 1$, the mean flow field is offshore directed with onshore directed. In comparison to the of Mr5b63 experiment, our results can produce the observed asymmetric steady circulation

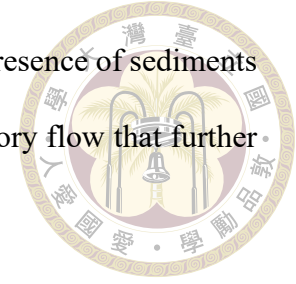


cells with high offshore mean flow up the lee slope and lower onshore mean flow up the stoss slope. Since the measured velocities on Mr5b63 are of sediment particles, van der Werf et al. (2007) claims it includes additional vertical velocities due to the sediment particles settling. This might be the reason the how our simulation cases under-estimated the vertical component on the resulting mean flow due to the absence of sediment particles in the control experiment.

However, even with the presence of sediments particles settling down the slope the mean flow of the 0.35 mm and 0.44 mm cases shows similar mean flow feature to the control case. This may due to the sediments limited area the sediment particles were distributed. By taking the mean flow of from $z = 0.205\text{m}$, the mean flow of this area showed that the circulation cells were higher on the stoss slope, upto $x/\lambda = -0.25$ and 0 for the 0.35 mm and 0.44 mm case. On the other hand the presence on 0.53 mm on the the cycle mean flow field showed a different flow pattern among the other simulation cases. The mean flow on stoss slope have a rather offshore directed flow while the mean flow on lee slope have a rather onshore directed flow. This onshore flow on lee slope surface extended until adjacent stoss slope at $x/\lambda = > 0.5$, causing the known onshore circulation cell at stoss slope be lifted $y/\eta = 0.25$ higher.

To further verify how the presence of sediment particles influence the flow we took the turbulent kinetic energy at $z = 0.205\text{m}$ for all experiment cases, as shown on Figure 3.12. The TKE for all cases is evident below the ripple crest, at $y/\eta < 0$. For the control case, there is high TKE near the surface of lee slope at $x/\lambda = 0.25$, which is due to the vortex-formation as shown on Figure 3.2. This high TKE on the lee side is further enhance with the presence of 0.35 mm and 0.44 mm sediments. As for the 0.44 mm case, the TKE is enhance up to the ripple trough at $x/\lambda = 0.5$. Consistently from the previous figures,

the 0.53 case showed the most varied result among all cases, as the presence of sediments at $x/\lambda = -0.5$ to 0.5, provided a consistent drag force to the oscillatory flow that further enhanced the TKE up to the adjacent ripple, from $x/\lambda = -1$ to 1.



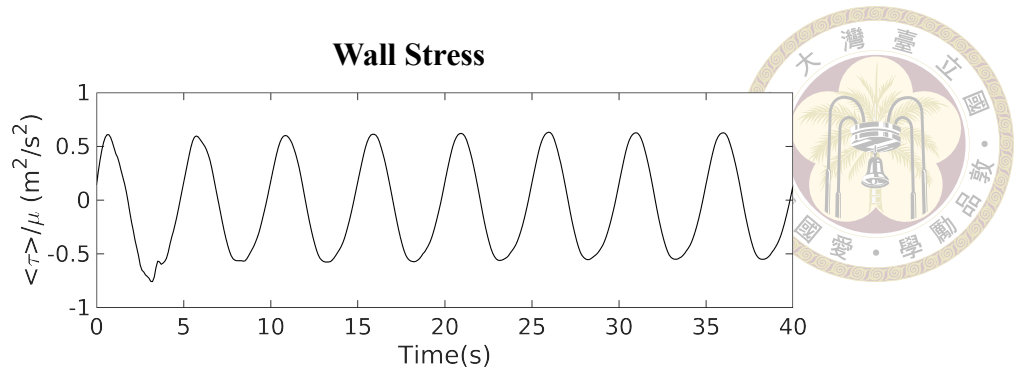


Figure 3.1: Time series of spanwise-average wall stress in the stream-wise direction. After one period the simulation reached quasi-steady solution.

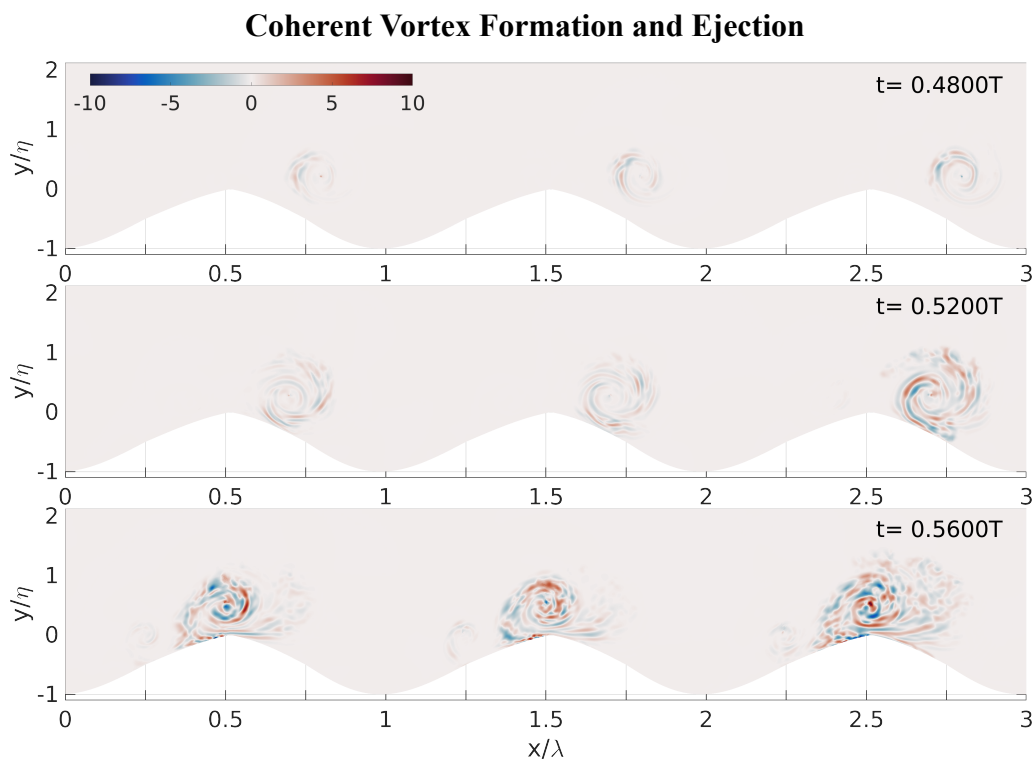


Figure 3.2: Snapshot of the instantaneous span-wise averaged vorticity on the first cycle. The formation of the vortex started at the lee slope at the end of the onshore flow $t = 0.48T$ and the ejection to the crest happened flow reversal $t = 0.52 T$.



Flow fields of the Mr5b63 laboratory experiment

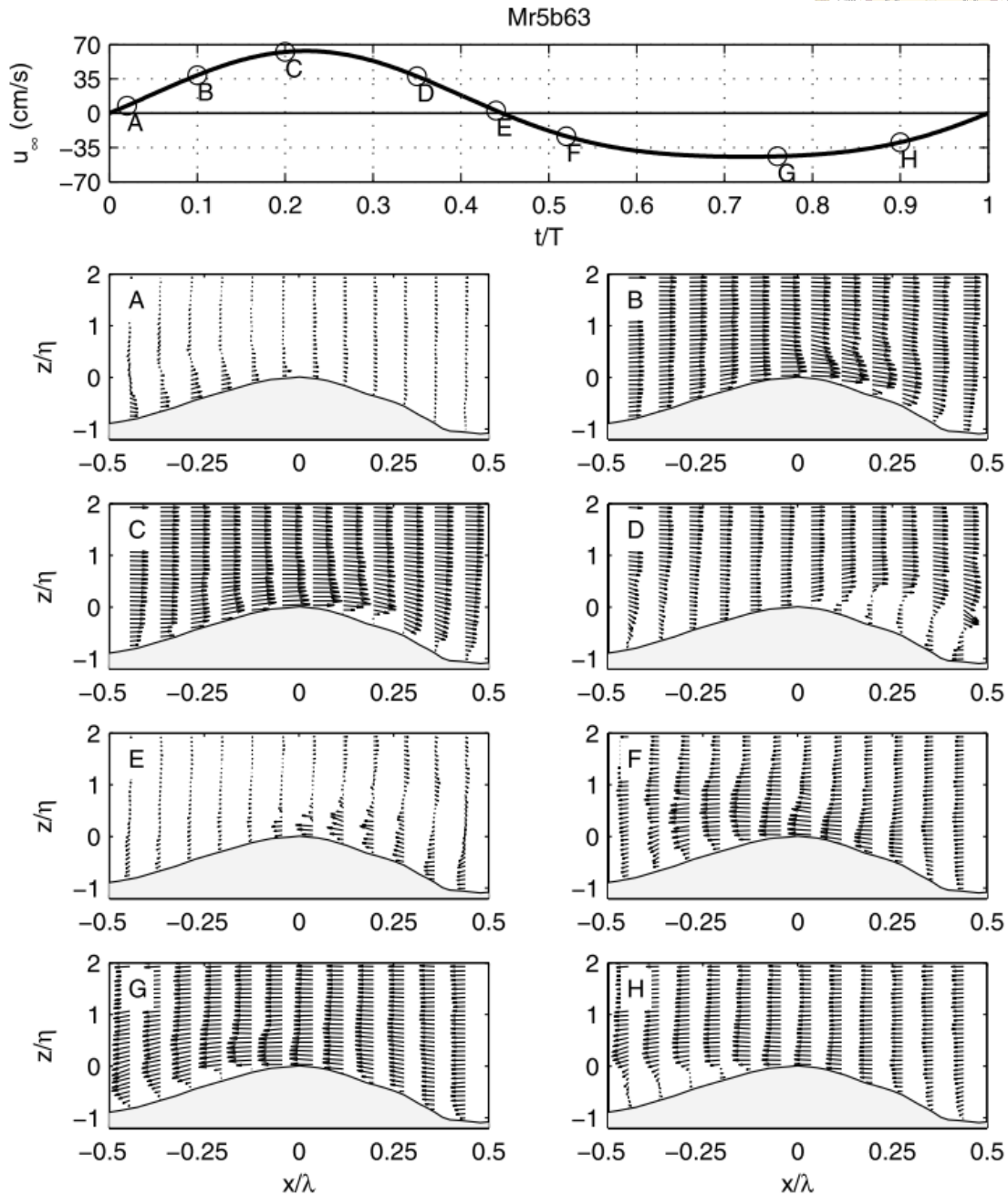
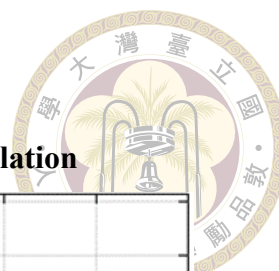


Figure 3.3: Flow field results of Mr5b63 laboratory experiment: Screenshot of Figure 1 on van der Werf et al. (2007). Top most panel is the calculated free-stream velocity, the letters corresponds to the t/T where following oscillatory velocity - flow feature occurs: (A) off-onshore flow reversal; (B) free stream is accelerating onshore; (C) maximum onshore free-stream velocity; (D) onshore free-stream velocity deceleration; (E) on-offshore flow reversal; (F) free stream acceleration offshore; (G) maximum offshore free stream velocity; and (H) offshore free-stream velocity deceleration.



Flow Field of the Control Case (No Sediments) Simulation

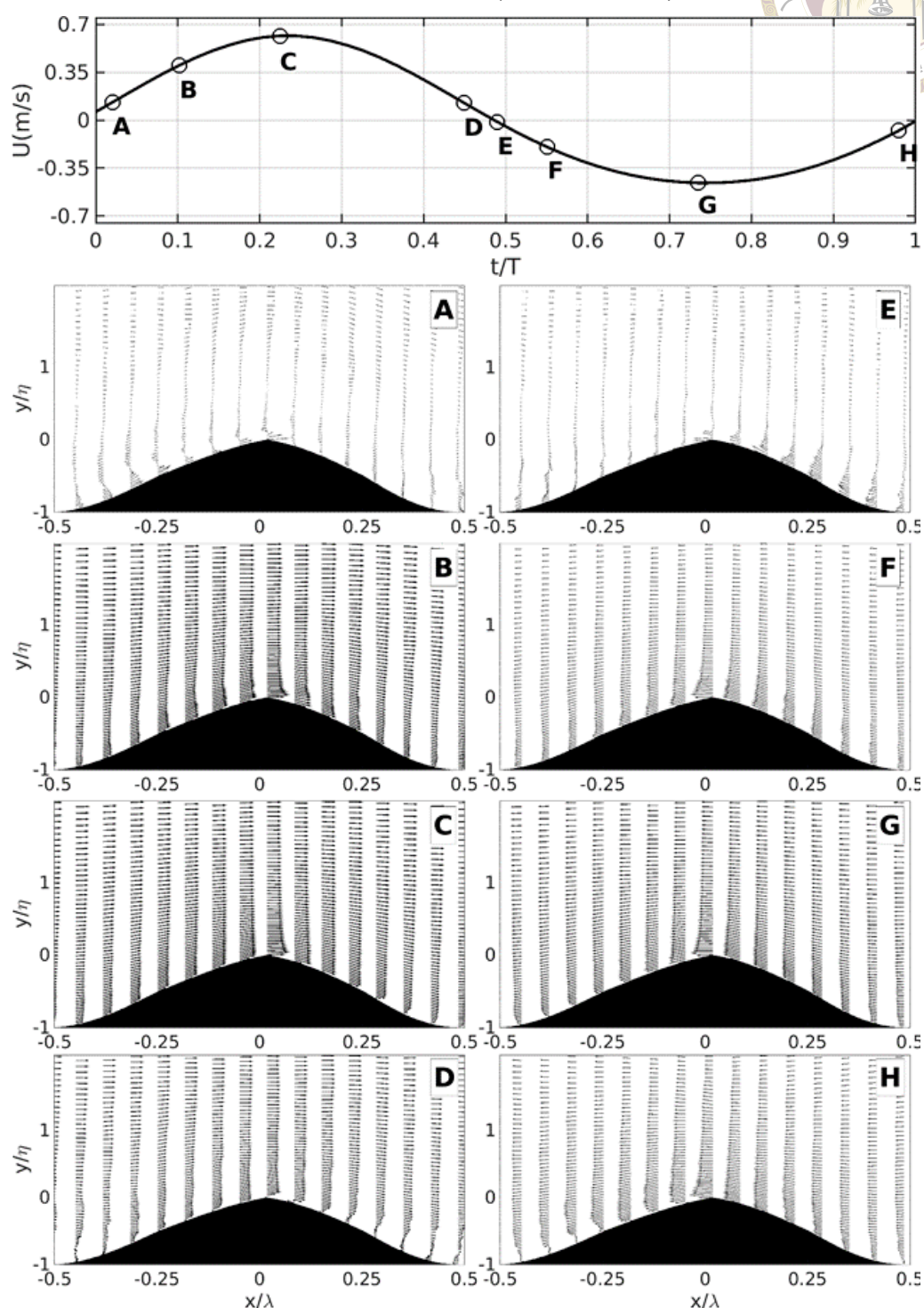
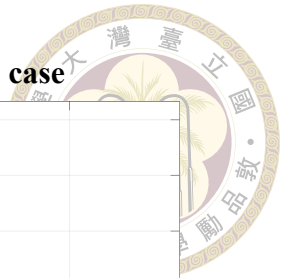


Figure 3.4: Top most panel is the calculated free-stream velocity with the letters (A) to (H) that corresponds to the approximate time of 8 flow features described in Figure 3.3. Panels (A) to (H) are the flow field results of the control case (no sediment) simulations.



Instantaneous Particle Volume Fraction for 0.35 mm case

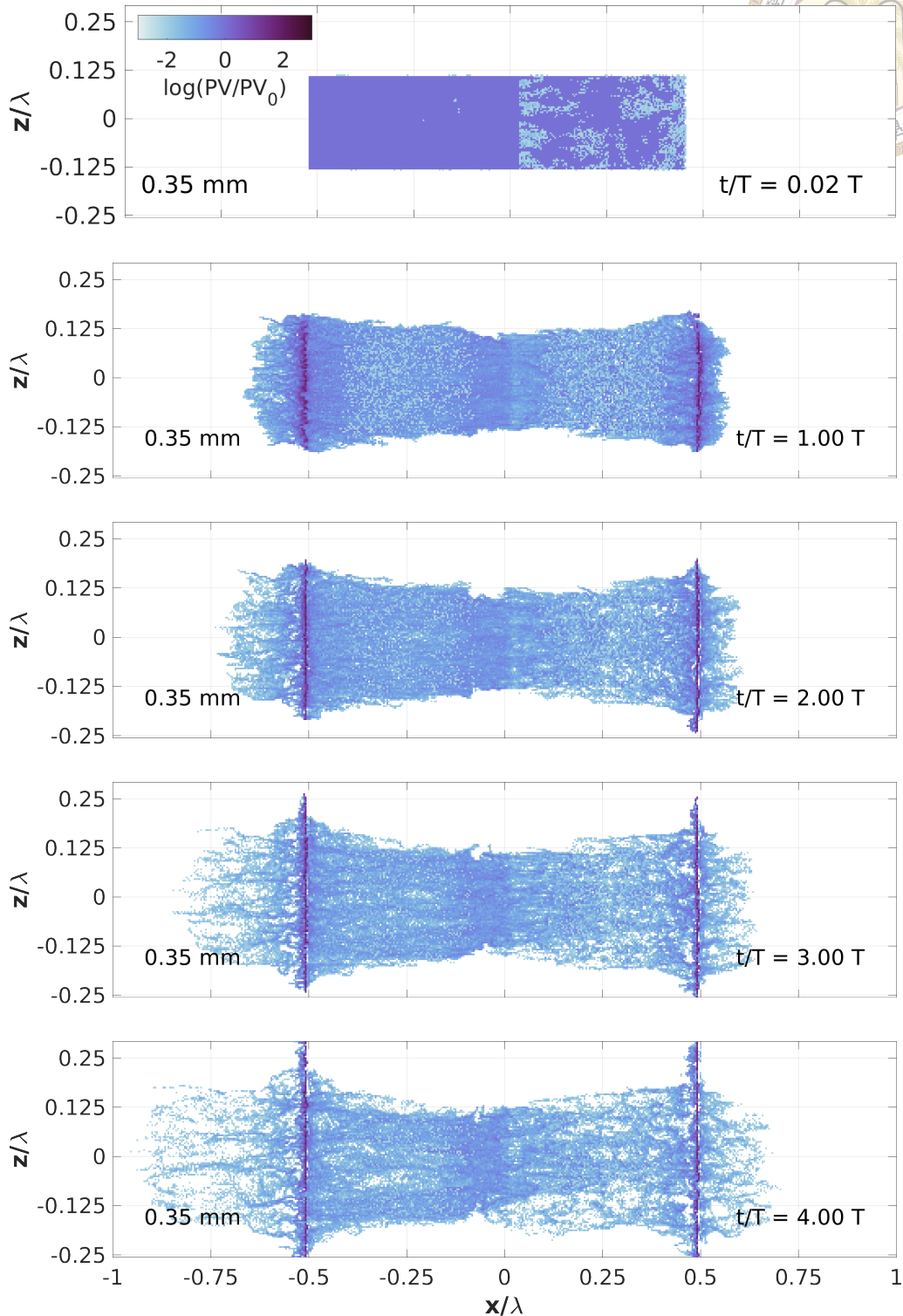


Figure 3.5: All panels are the top view of the particle volume fraction for 0.35 mm case at five instances: at $t/T = 0.02, 1, 2, 3,$ and 4 - the initial result followed by the results at end of every oscillatory flow period. The color represents the logarithmic particle volume fraction normalize by the initial particle volume value. The initial value is at $t/T = 0.02$, is almost to zero as values are close to the initial particle volume value. The lighter shade means the particle volume fraction is lower from the initial value, the darker shade means the particle volume fraction is higher from from initial value.



Instantaneous Particle Volume Fraction for 0.44 mm case

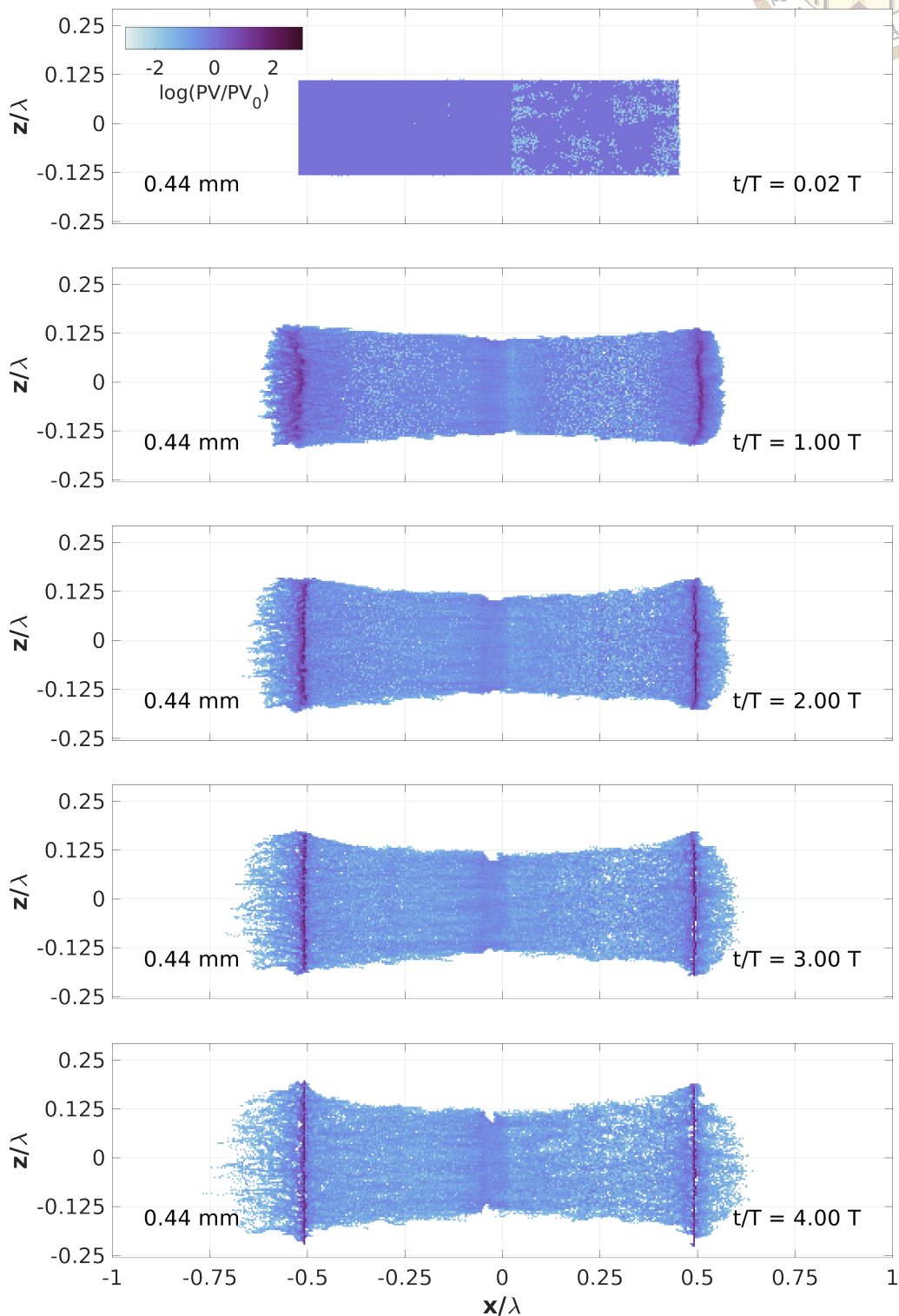
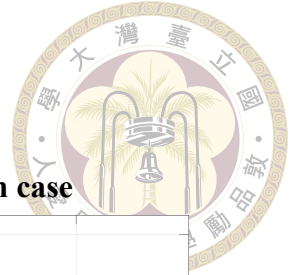


Figure 3.6: Same as Figure 3.5 but for 0.44 mm case.



Instantaneous Particle Volume Fraction for 0.53 mm case

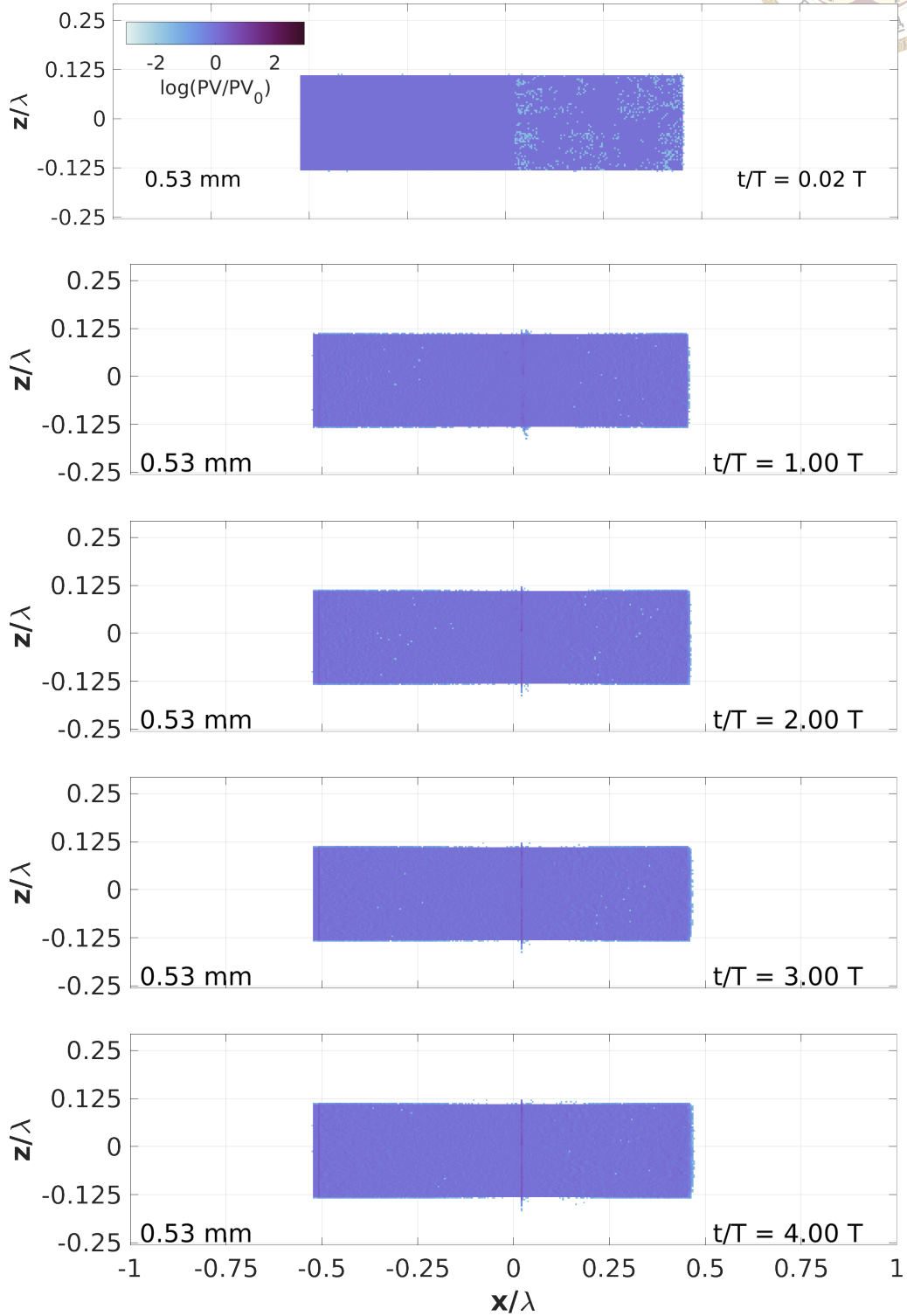


Figure 3.7: Same as 3.5 but for 0.53 mm case.

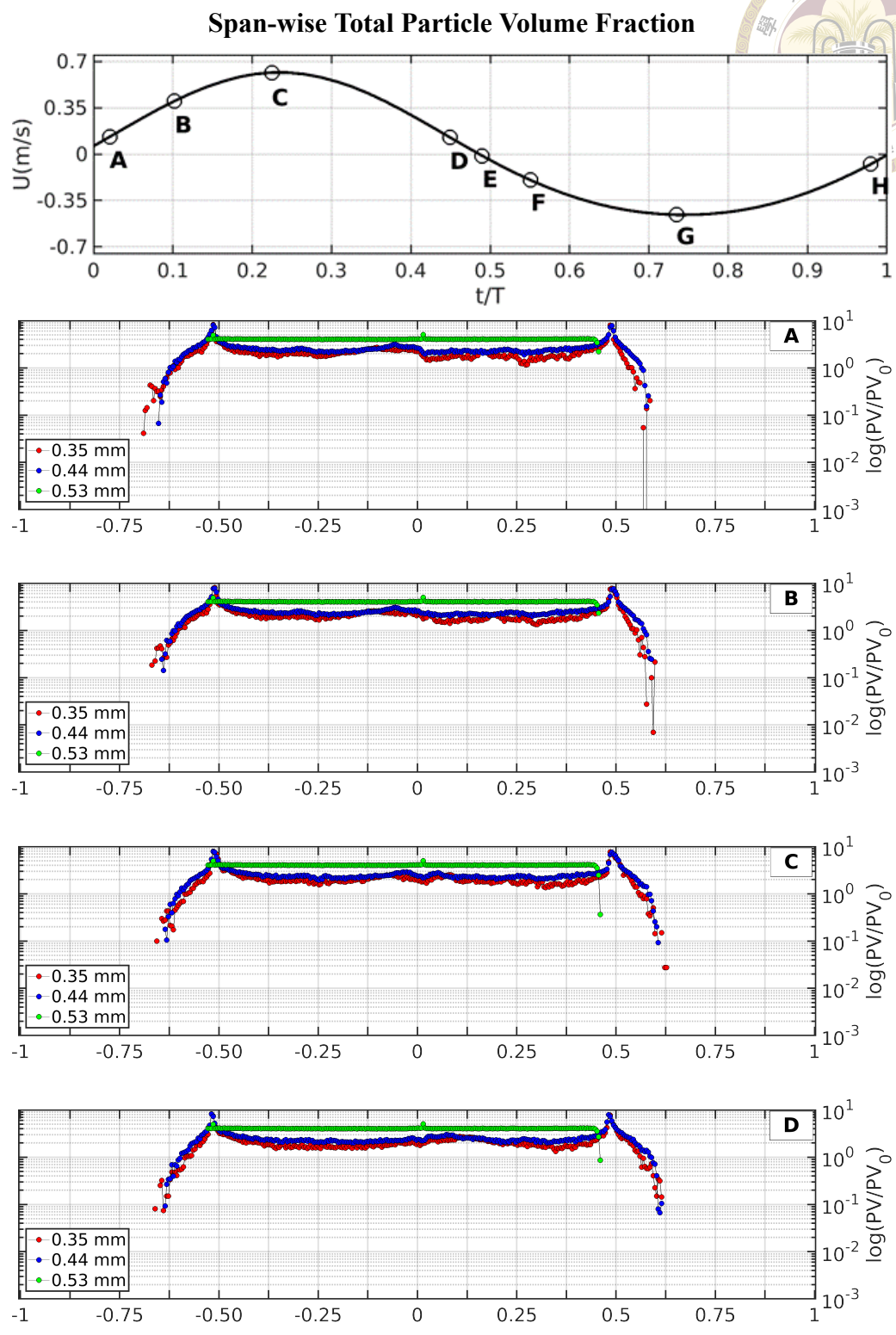
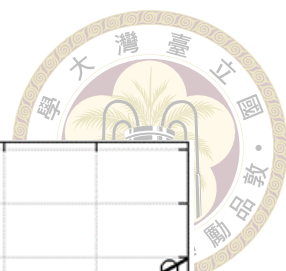


Figure 3.8: Top most panel is the calculated free-stream velocity with the letters (A) to (H) that corresponds to the $\approx t/T$ of 8 flow features described in Figure 3.3. Panels (A) to (H) are the span-wise total particle volume fraction for all cases. Red marker represents the 0.35 mm case, blue marker represents the 0.44 mm case and green marker represents the 0.53 case.

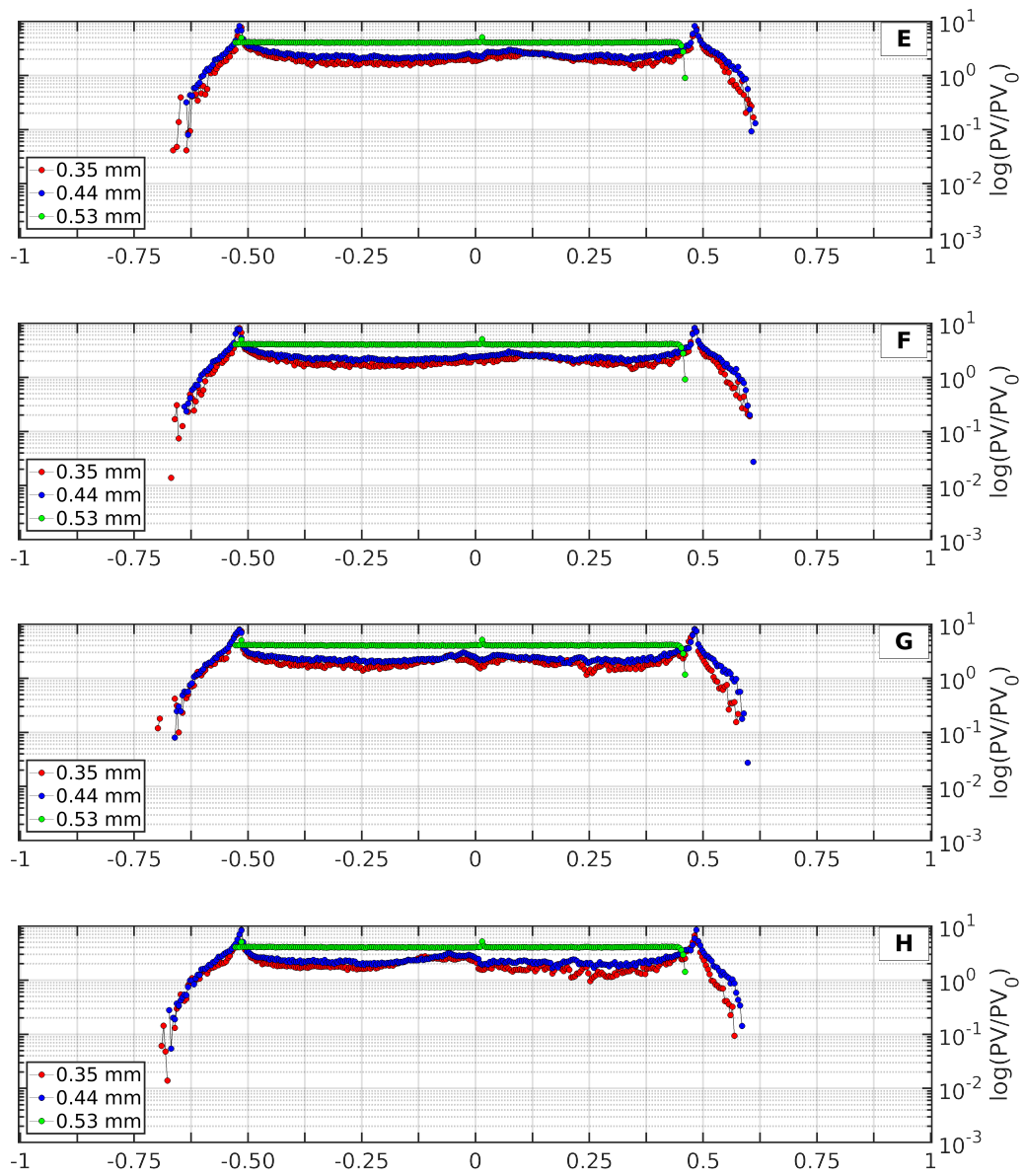


Figure 3.9: Continued.

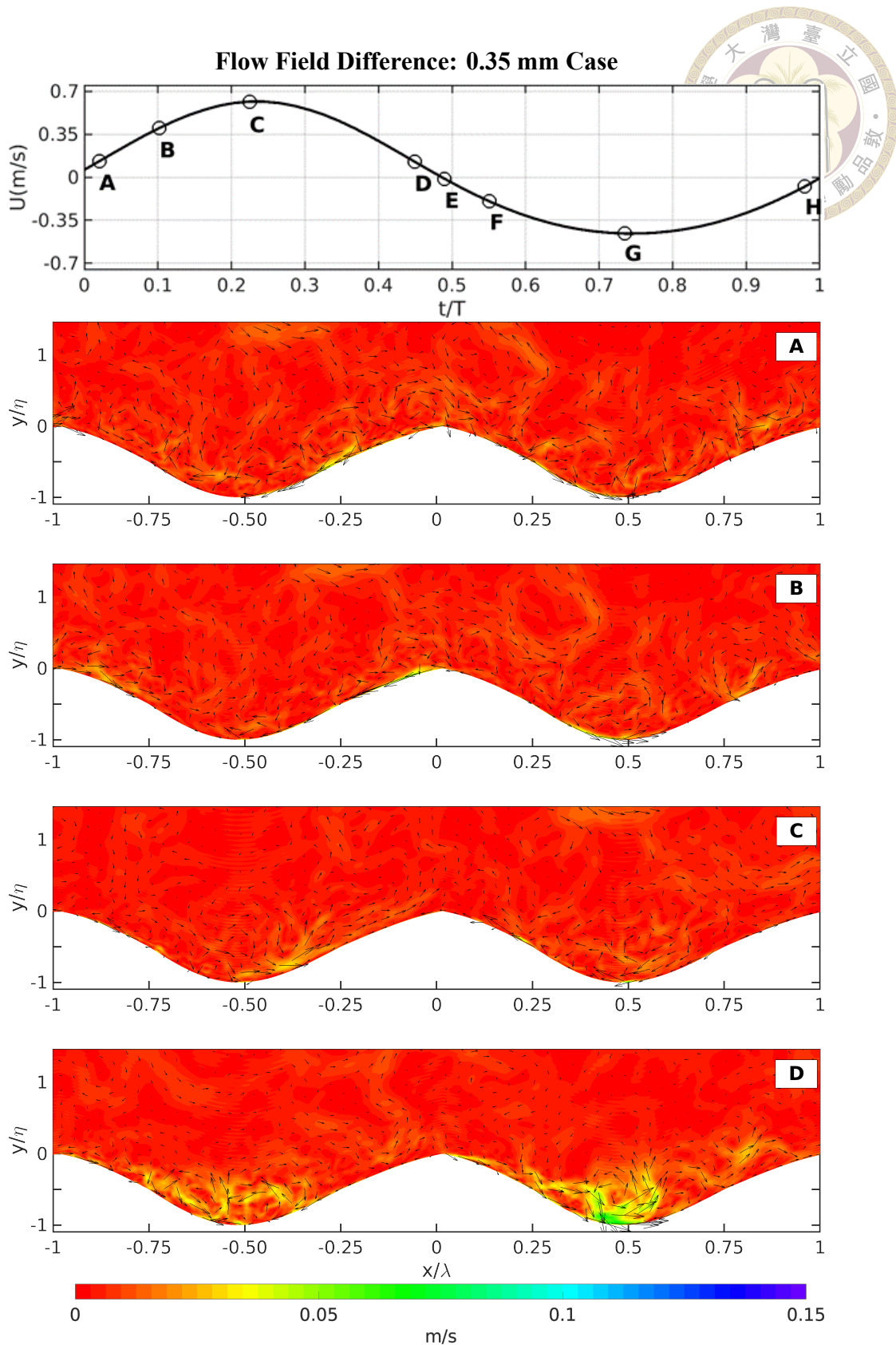


Figure 3.10: Top most panel is the calculated free-stream velocity with the letters (A) to (H) that corresponds to the $\approx t/T$ of 8 flow features described in Figure 3.3. Panels (A) to (H) are the flow field difference results between the 0.35 mm case and control case (no sediment) simulations. The color represent the magnitude overlaid with the corresponding velocity vectors.

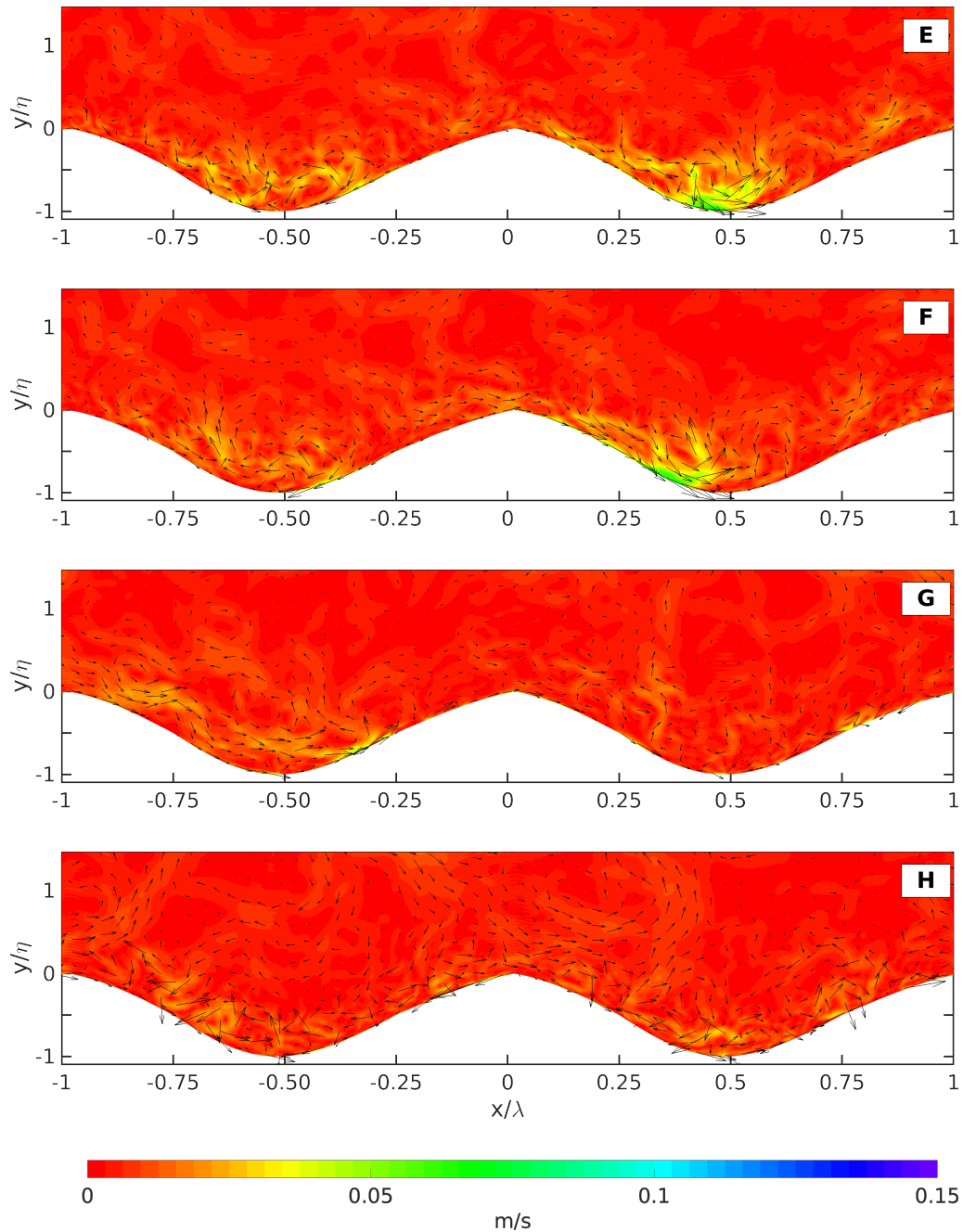
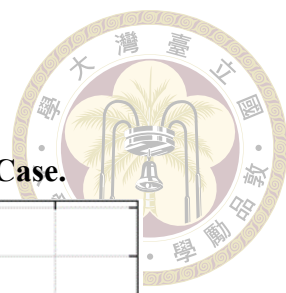


Figure 3.10: Continued.



Flow field difference of 0.44 mm Case and Control Case.

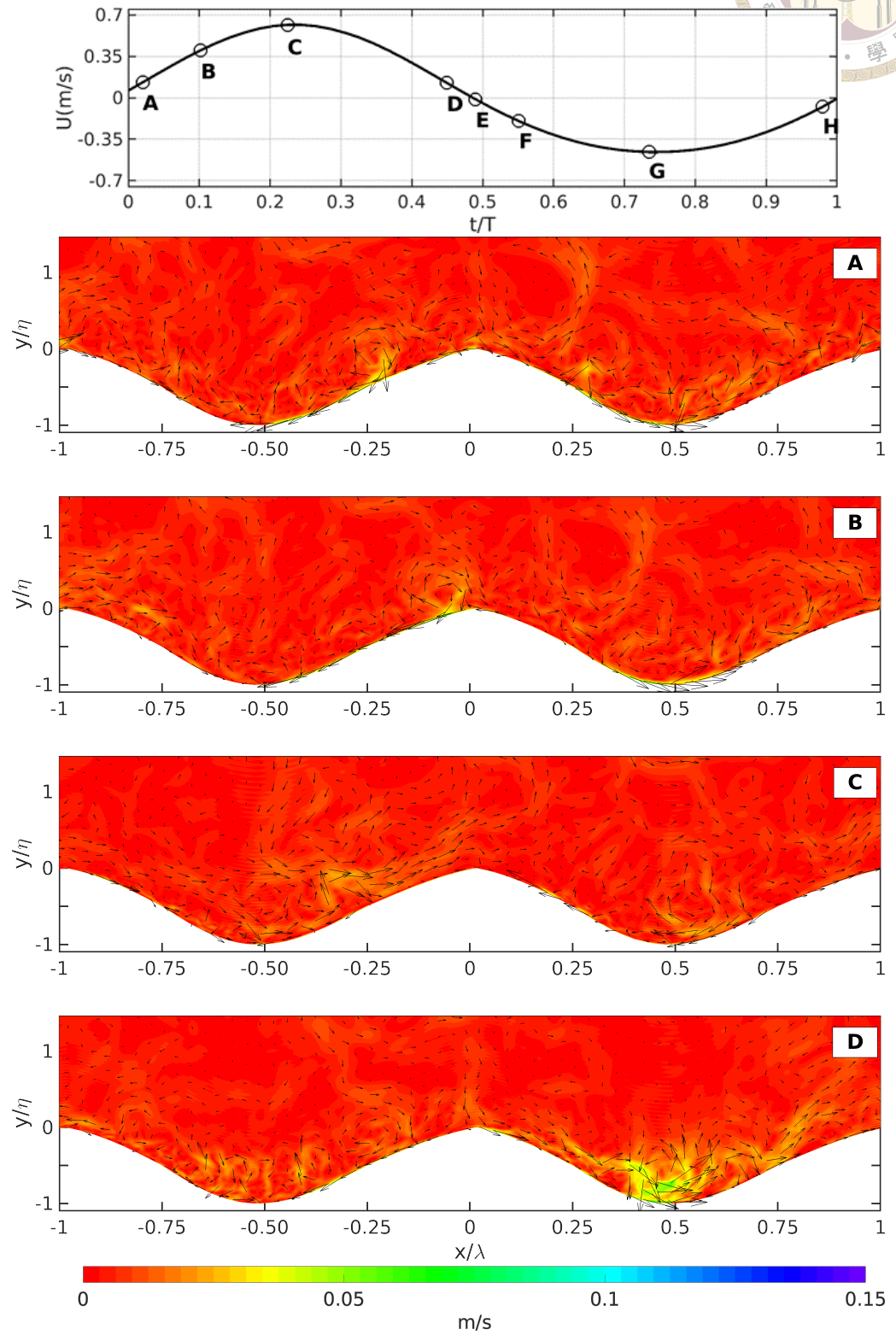


Figure 3.11: Same as Figure 3.10 but for 0.42 mm case.

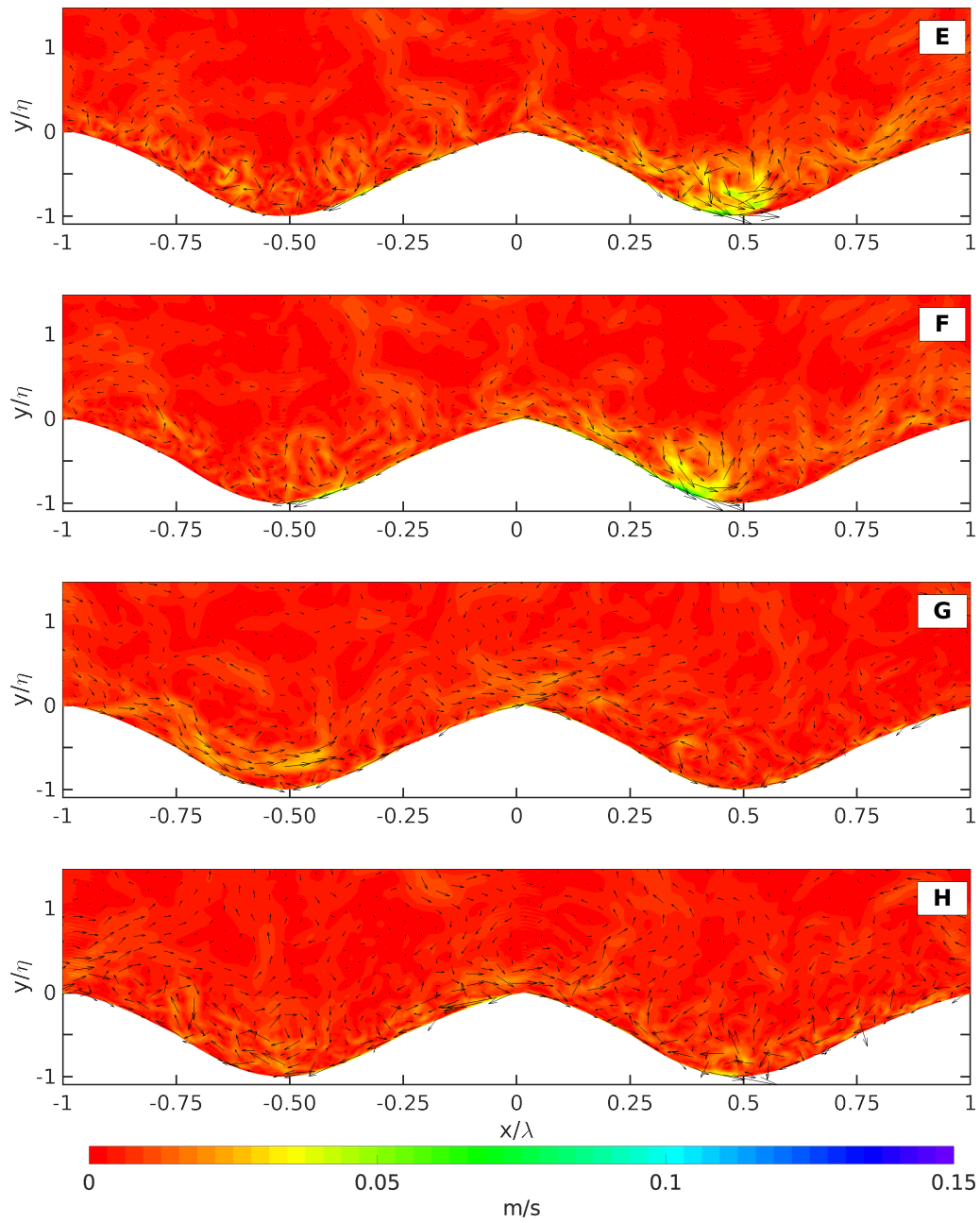


Figure 3.11: Continued.



Flow field difference of 0.53 mm Case and Control Case.

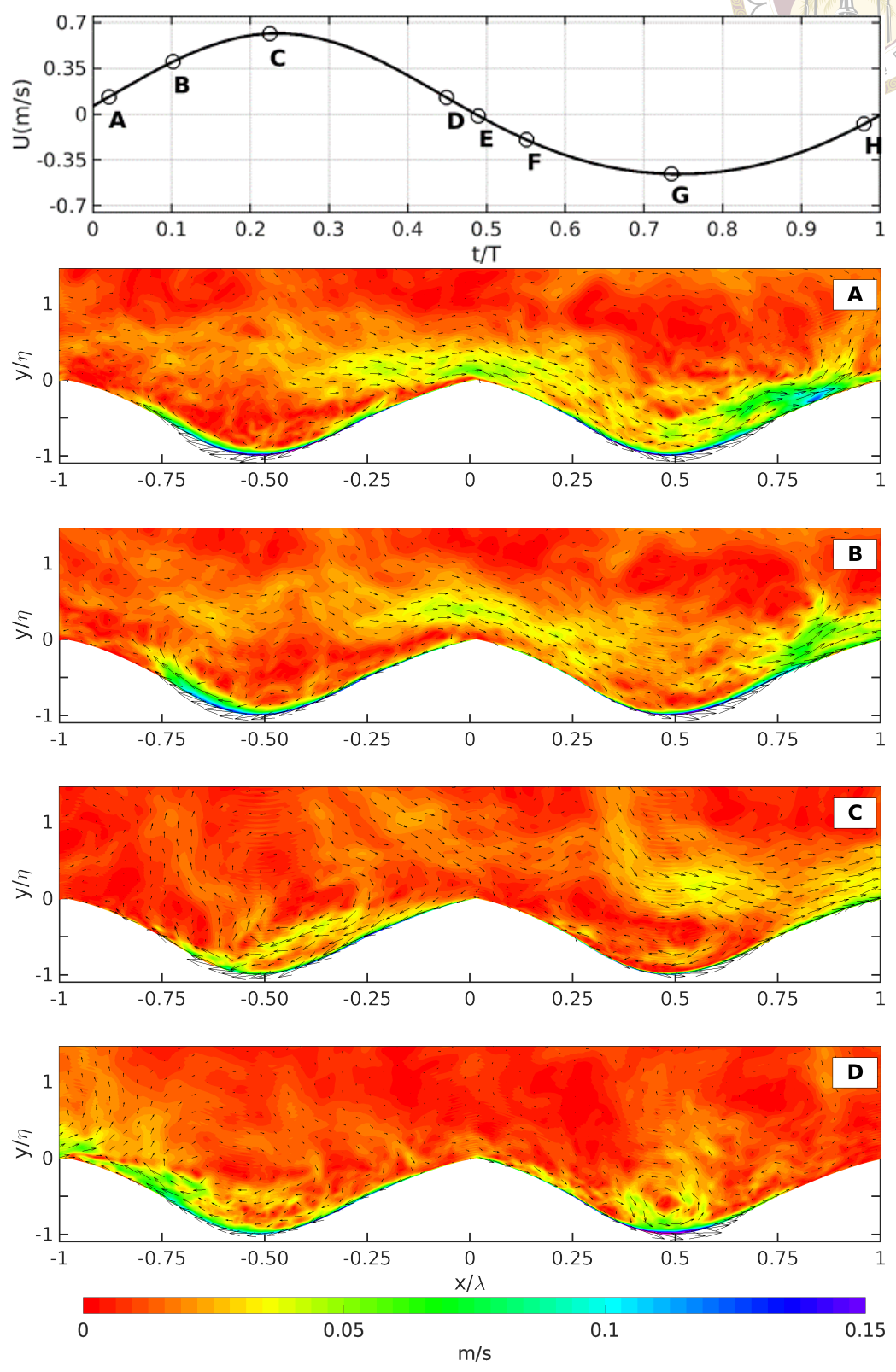


Figure 3.12: Same as Figure 3.10 but for 0.53 mm case.

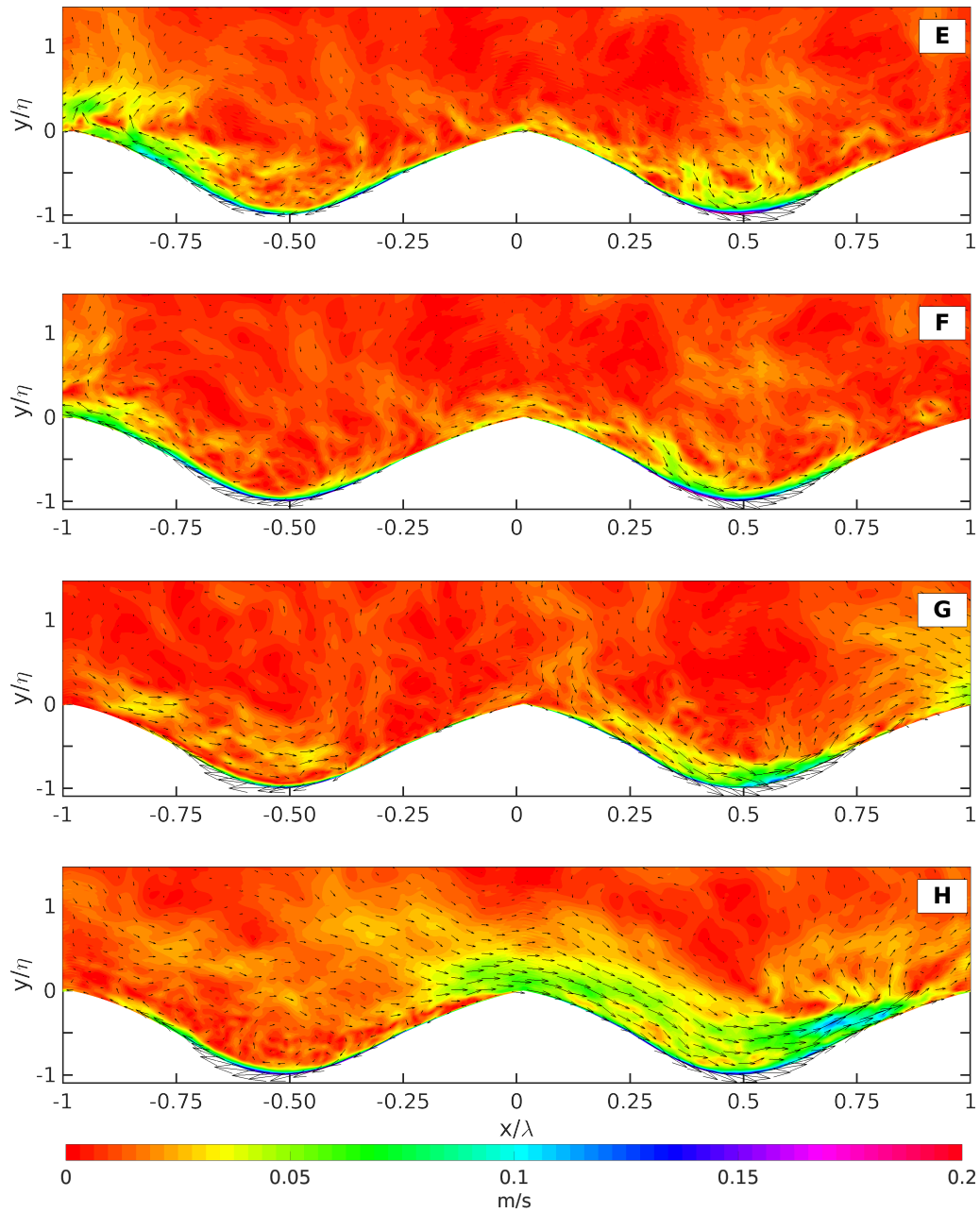


Figure 3.12: Continued.

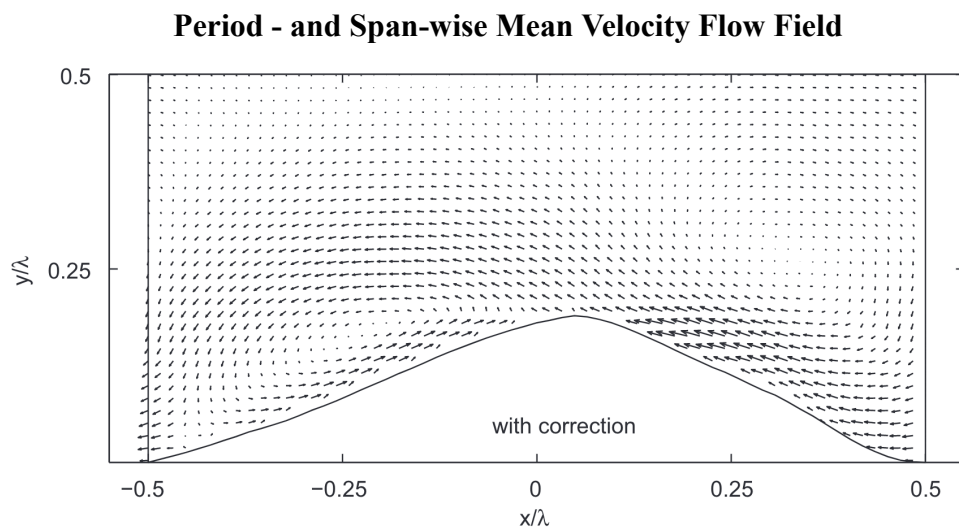


Figure 3.12: Period- and spanwise- mean velocity flow field based on Mr5b63 experiment of van der Werf et al. (2007): Screenshot of Figure A1 on van der Werf et al. (2008).



Period - and Span-wise Velocity Flow Field

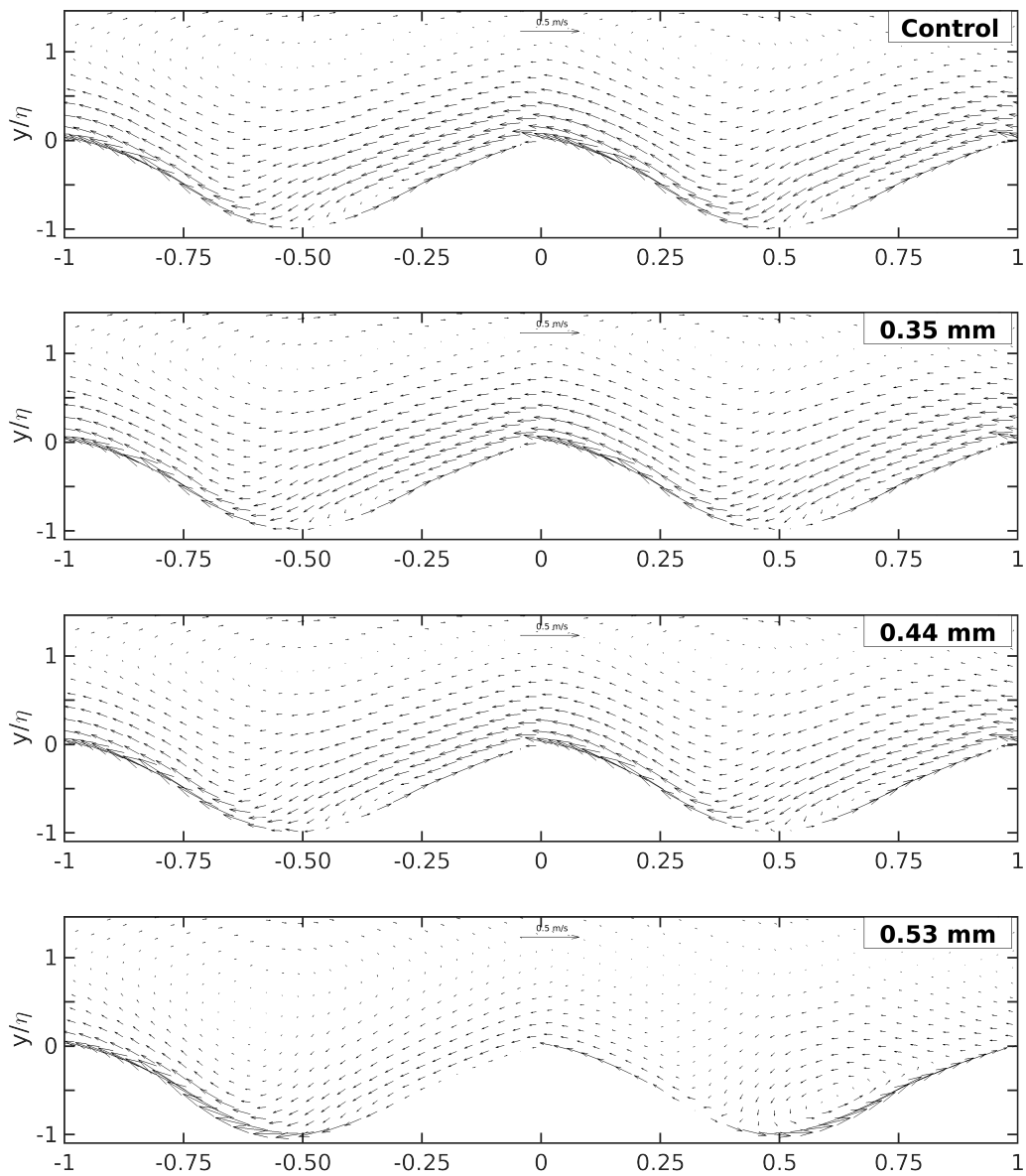


Figure 3.12: Top-most panel is the control case followed by the simulation cases with sediments - 0.35 mm case, 0.44 mm case and 0.53 mm case.

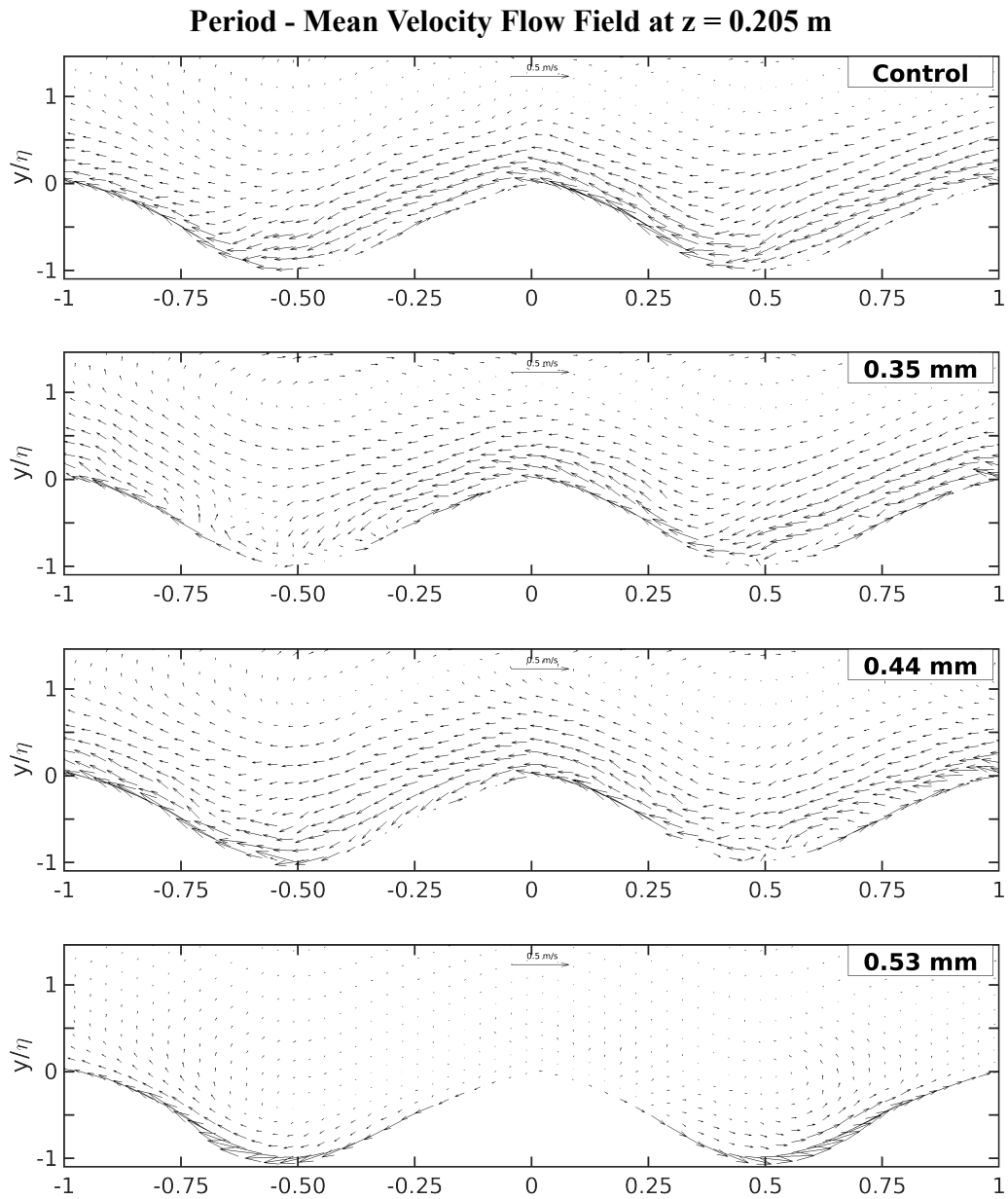


Figure 3.12: Top-most panel is the control case followed by the simulation cases with sediments - 0.35 mm case, 0.44 mm case and 0.53 mm case.



Turbulent Kinetic Energy at $z = 0.205$ m

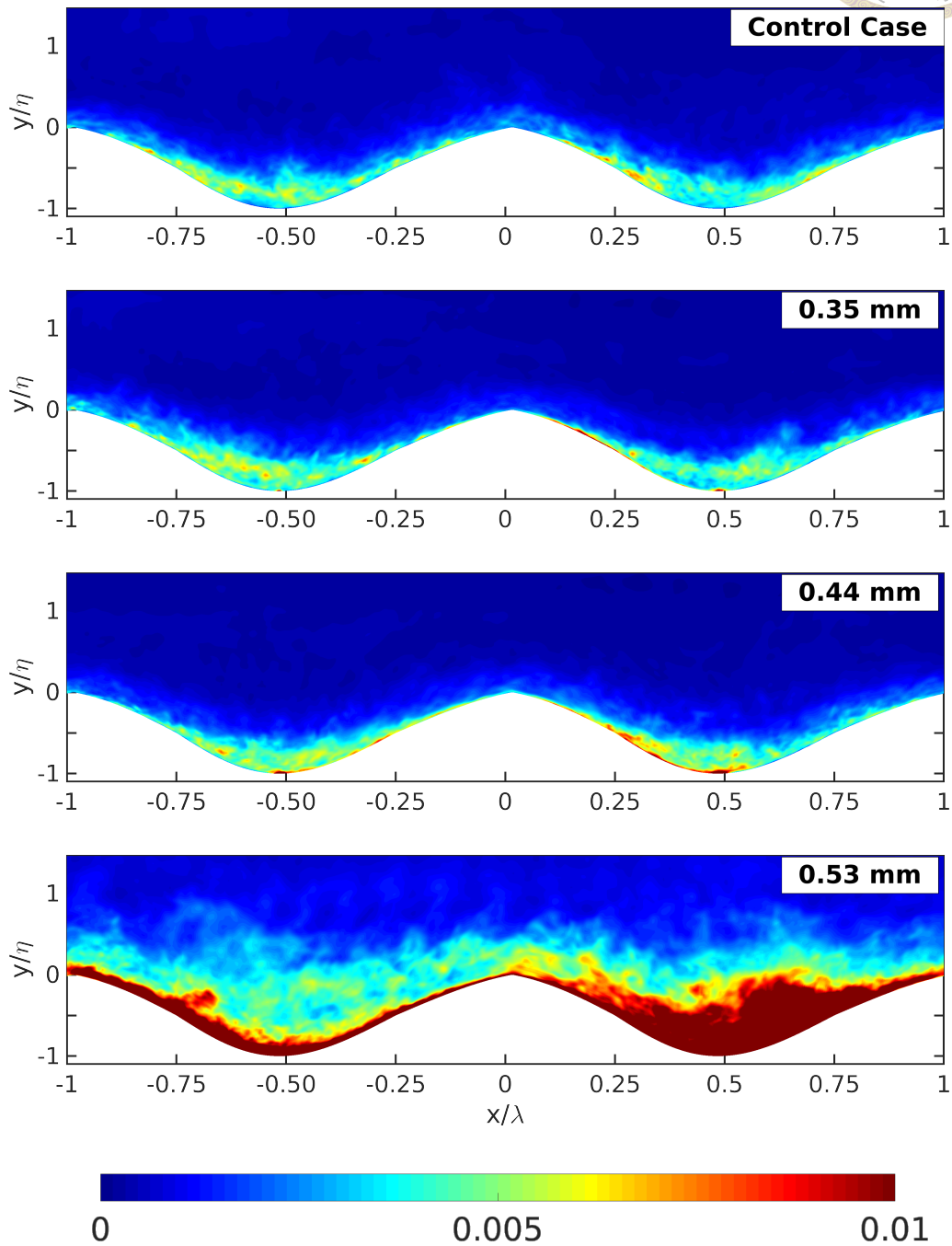


Figure 3.12: Top-most panel is the control case followed by the simulation cases with sediments - 0.35 mm case, 0.44 mm case and 0.53 mm case.



Chapter 4 Discussion

To further understand the effect of sediment particle presence on the oscillatory flow field, presented in this section is some energy budget equation adopted from Chou and Shao (2016). The total kinetic energy of the system is calculated using the following equation:

$$KE_{tot} = \int_{t=0}^{4T} \frac{d}{dt} \int_V \frac{1}{2} \rho_0 |\mathbf{u}_{osc}|^2 dV dt + \int_{t=0}^{4T} \frac{d}{dt} \sum_{n=1}^{N_{sed}} \frac{1}{2} m_{sed} |\mathbf{u}_{sed}|^2 dt \quad (4.1)$$

where the first term on the RHS is the total kinetic energy of the oscillatory flow evaluated over the control volume and the second term is the total kinetic energy of the sediment particles. Figure 4.1 shows the calculation result from Eq.4.1. Top panel shows the KE_{tot} for the control case, middle panels shows the result for the simulation cases with sediments, and last panel is the difference of cases with sediments and the control case. For all experiment the dominant forcing is the oscillatory flow with the kinetic energy is higher during the onshore flow and lower than the offshore flow. The presence of the sediment showed an increasing contribution to the KE_{tot} of each the system. The energy contribution of the 0.35 mm and 0.44 mm case is in-phase as the oscillatory flow and increasing in magnitude gradually over time. While the 0.53 mm have a varying energy contribution that coincides with peaks during the maximum offshore flow, but

lowest during the maximum onshore flow. To verify the range of the difference of the KE_{tot} of the simulation cases with the sediment and control case, we calculated the we calculated turbulent kinetic energy (TKE) using Reynolds averaging by substituting \mathbf{u}_{osc} on Equation (4.1) with:

$$\mathbf{u}'_{osc} = \mathbf{u}_{osc} - \bar{\mathbf{u}}_{osc}, \quad (4.2)$$

where $\bar{\mathbf{u}}$ span-wise mean of the oscillatory flow. Figure 4.2 shows the resulting plot of the time series of the TKE for all the simulation cases. Upon initializing the sediment particles at $t/T = 0$, all cases started with the same value and diverge in trend before the first flow reversal $t/T = 0.4$, - with the 0.53 mm case having an increasing trend, while the 0.35 mm case and 0.44 mm case having a constant trend. After two cycles, 0.35 mm case and 0.44 mm case have the same trend with each other, where the having TKE decreases during the flow reversal and increasing during the maximum onshore and offshore flow. Likewise, the flow asymmetry is also reflected on the TKE where the maximum onshore flow is higher than the maximum offshore flow, although there is an obvious delay on the TKE plot. On the other hand the 0.53 mm case shows that the TKE decreases during the off-onshore reversal and increases during the maximum onshore flow and the maximum offshore flow.

To quantify how the particle motion contribute to the energy or release of potential energy, we used the following the equation for ΔPE_{sed} :

$$\Delta PE_{sed} = \int_{t=0}^{4T} \frac{d}{dt} \sum_{n=1}^{N_{sed}} \frac{1}{2} \mathbf{u}_{sed,n} \cdot m_{sed} \left(1 - \frac{1}{s}\right) \mathbf{g} \quad (4.3)$$

The corresponding plot of the equation above for all cases is shown in Figure 4.3. The

trend 0.35 mm and 0.44 mm confirms how the finer sediments were able to follow the oscillatory flow, as the same phase as the oscillatory flow, but there is an decrease in magnitude, as the sediments were accumulated at the ripple trough and distributed spanwise. The calculation result of ΔPE_{sed} for 0.53 mm case also confirms our results on Figure 3.7 of having the almost no particle movement throughout the simulation.

Although the 0.53 mm case almost have no particle movement, it has a highest TKE among the other case, thus we took a look at the inter-phase drag - a mechanism that could dissipate the release of potential energy with the us of the following equation:

$$Drag_{sed} = \int_{t=0}^{4T} \frac{d}{dt} \sum_{n=1}^{N_{sed}} m_{sed} \frac{|\mathbf{u}_{sed,n} - \mathbf{u}_{osc|sed,n}|^2}{\tau_{sed}} dt \quad (4.4)$$

The corresponding plot of the equation above for all cases is shown in Figure 4.4. Upon initialization there is a high drag for 0.35 case and 0.44 mm on case , this decreased over time after the first $t/T = 1$ as the sediments move down the slope. On the contrary, the high drag calculation result for 0.53 mm is constant over four periods, since the particle volume distribution is the same over time as shown on Figure 3.7. This constant high drag contribution from 0.53 mm enhanced the TKE seen on Figure 4.2. In comparison to ΔPE_{sed} calculation the $Drag_{sed}$ calculation is two orders higher, which shows that in our simulation case the interphase drag has higher contribution to the energy budget than of particle motion or particle entrainment.

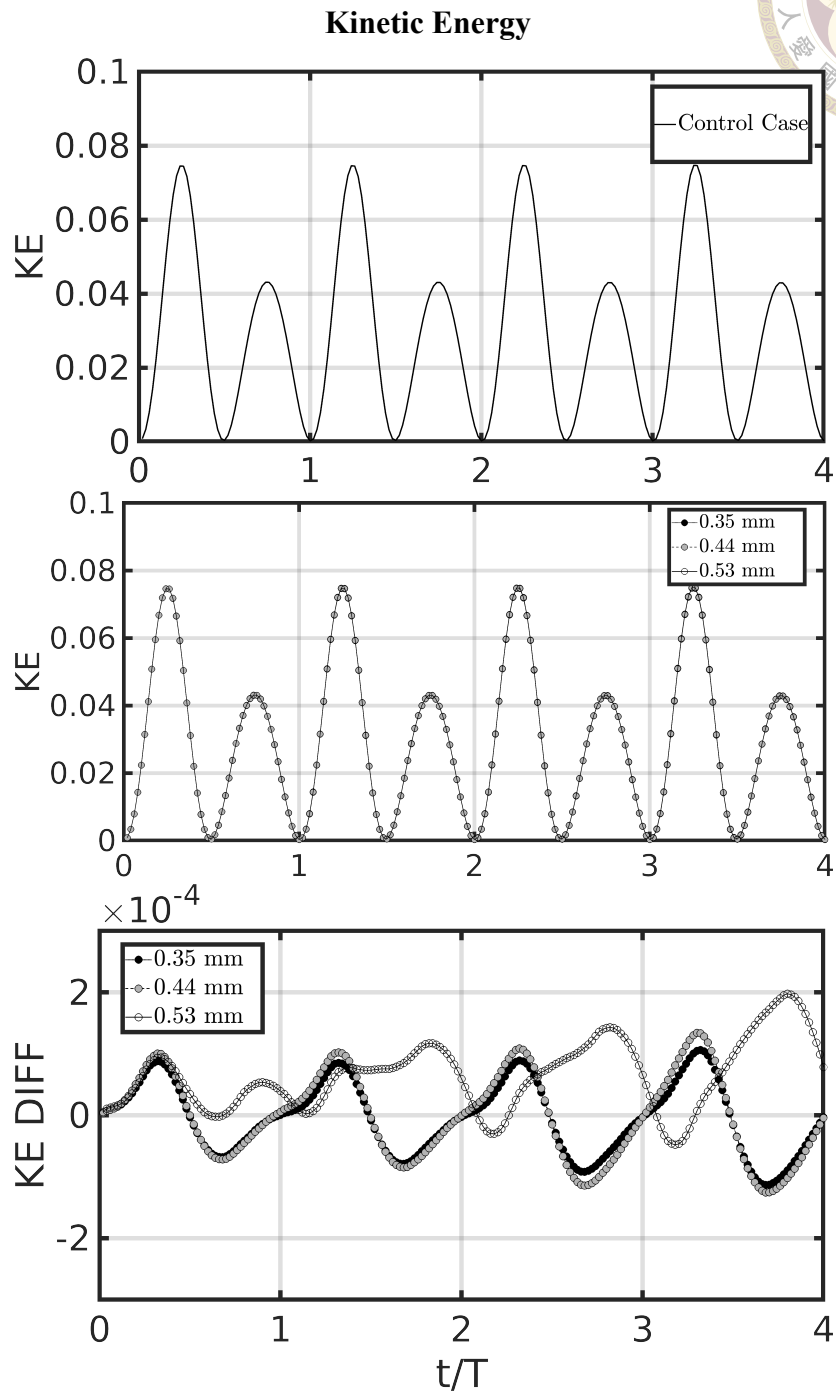
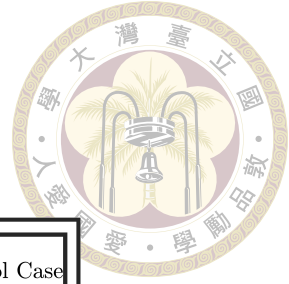


Figure 4.1: Top panel is the time series of the total kinetic energy for control case. Middle panel is the time series of the total kinetic energy for the simulation case with sediments. Note that there are three lines plotted on this panel. Last panel is the difference of the second and first panel. Black-filled marker is for 0.35 mm case, gray-filled marker is for 0.44 mm case and white-filled marker is for 0.53 mm case.

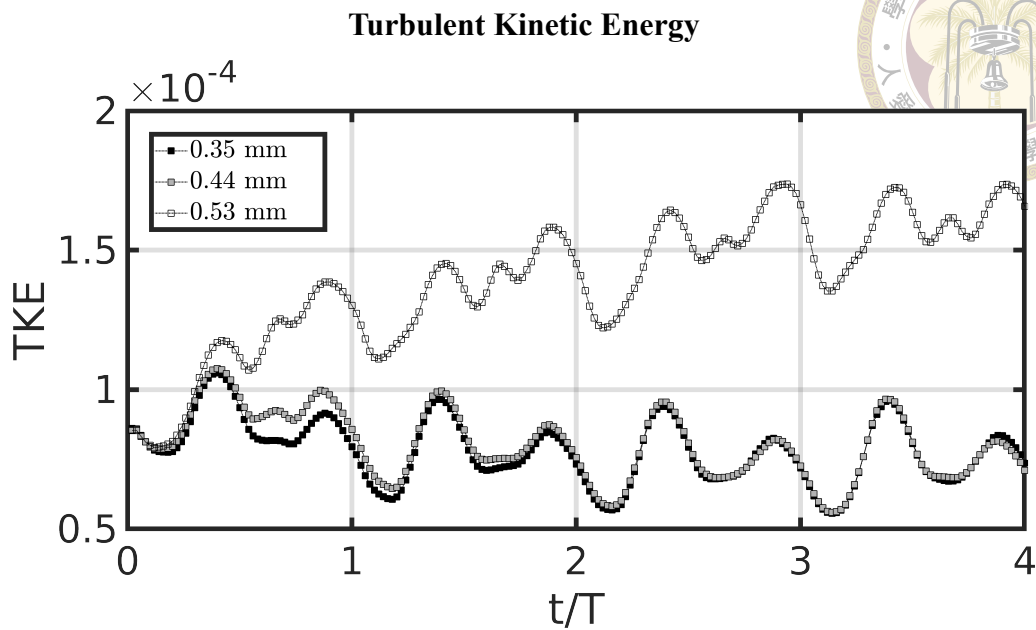


Figure 4.2: Time series turbulent kinetic energy for all three cases. Black-filled marker is for 0.35 mm case, grey-filled marker is for 0.44 mm case and white-filled marker is for 0.53 mm case.

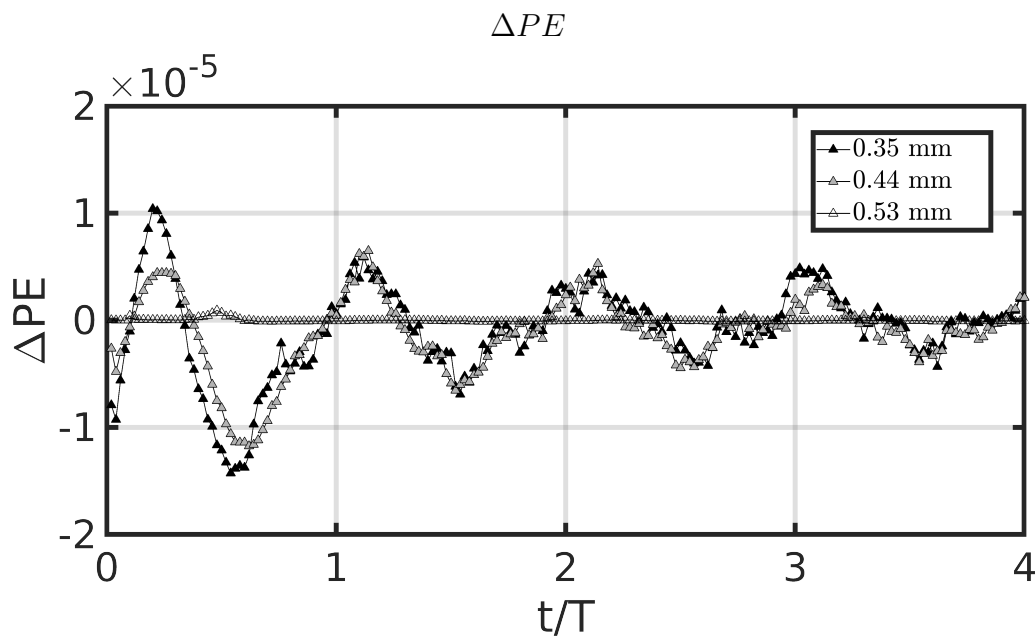


Figure 4.3: Time series ΔPE due to the motion of sediment particles for all three cases. Black-filled marker is for 0.35 mm case, grey-filled marker is for 0.44 mm case and white-filled marker is for 0.53 mm case.

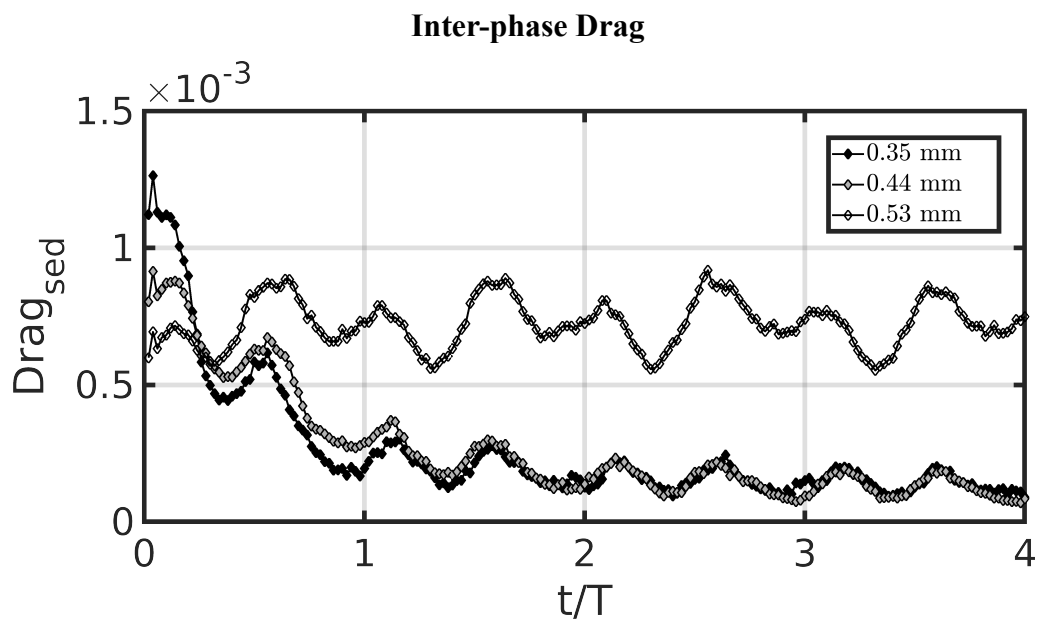



Figure 4.4: Time series of energy dissipation due to inter-phase drag for all three cases. Black-filled marker is for 0.35 mm case, gray-filled marker is for 0.44 mm case and white-filled marker is for 0.53 mm case



Chapter 5 Summary

To investigate the role of sediment particle motion and particle-related interphase drag on an oscillatory flow over ripples we conducted four numerical simulations of a vortex ripple based on the flow conditions and ripple dimension of the Mr5b63 laboratory experiment of van der Werf et al. (2007), using the Euler-Lagrange model of Chou et al. (2015). The four cases are as follows: control (no sediment), 0.35 mm, 0.44 mm and 0.53 mm. The control case served as a baseline to compare the other simulation cases with sediments. All simulation cases with sediments have the same bulk particle volume value introduced at the first grid of vortex ripple. The control case simulation, even without the sediments, can capture the coherent vortex formation and ejection, and in good agreement with known observed flow pattern features. With the presence of sediment particles, the simulation results showed that cases with finer sediments (0.35 mm and 0.44 mm), moved down the ripple slope and accumulated at the ripple through, entrained with oscillatory flow but does not have significant difference with time dependent and time average velocity fields except during the flow reversal. The case with coarser particles (0.53 mm) neither have significant particle motion and nor entertainment with oscillatory flow but have significant difference with time dependent and time average velocity fields. The energy calculation showed total kinetic energy is dominated by the asymmetric oscillatory flow induced through pressure gradient force. The total kinetic energy difference of cases




with point particles from control case showed that the increasing trend for all the cases. The cases with finer particles (0.35 mm and 0.44 mm) have the same trend as the oscillatory flow, while the case with coarse particles (0.53 mm) increases during offshore and decelerates during onshore. The calculated TKE showed that the 0.35 mm and 0.44 mm case are in-phase as the total kinetic energy and are in equilibrium after two flow period, while the 0.53 mm case is increases at flow reversal and peaks during the maximum offshore flow. The calculated ΔPE showed that the 0.35 mm and 0.44 mm case are in phase as the oscillatory flow, decreases in magnitude over time, while there is close to zero ΔPE or no motion for the 0.53 mm case. The calculated interphase drag are two order higher than ΔPE . The results showed the 0.35 mm and 0.44 mm case decreased in magnitude after first flow period, not affected by flow asymmetry, while 0.53 mm case peaks during off-offshore flow reversal, lowest during maximum onshore flow. Although the simulation could further be improved by incorporating forcing due to sediment collision, our study still confirms the caution of considering a single sediment particle size for drag contribution as the basis for computation of grain-related roughness used for grain-related bed shear stress for sediment transport calculation.



References

- Amoudry, L. O. and A. J. Souza (2011). Deterministic coastal morphological and sediment transport modeling: A review and discussion. *Reviews of Geophysics* 49(2), 1–21.
- Blondeaux, P. (1990). Sand ripples under sea waves part 1. ripple formation. *Journal of Fluid Mechanics* 218, 1–17.
- Blondeaux, P. and G. Vittori (1991). Vorticity dynamics in an oscillatory flow over a rippled bed. *Journal of Fluid Mechanics* 226, 257–289.
- Brakenhoff, L., R. Schrijvershof, J. van der Werf, B. Grasmeyer, G. Ruessink, and M. van der Vegt (2020, 11). From ripples to large-scale sand transport: The effects of bedform-related roughness on hydrodynamics and sediment transport patterns in delft3d. *Journal of Marine Science and Engineering* 8, 1–25.
- Chen, X. and X. Yu (2015). A numerical study on oscillatory flow-induced sediment motion over vortex ripples. *Journal of Physical Oceanography* 45, 228–246.
- Cherlet, J., G. Besio, P. Blondeaux, V. V. Lancker, E. Verfaillie, and G. Vittori (2007). Modeling sand wave characteristics on the belgian continental shelf and in the calais-shyphen; dover strait. *Journal of Geophysical Research* 112, 6002.

- 
- Chou, Y. J., S. H. Gu, and Y. C. Shao (2015). An Euler-Lagrange model for simulating fine particle suspension in liquid flows. *Journal of Computational Physics* 299(1), 955–973.
- Chou, Y. J. and Y. C. Shao (2016). Numerical study of particle-induced Rayleigh-Taylor instability: Effects of particle settling and entrainment. *Physics of Fluids* 28(4).
- Cui, A. (1999). *On Parallel Computation of Turbulent Rotating Stratified Flows*. Ph. D. thesis.
- Dimas, A. A. and G. A. Leftheriotis (2019). Mobility Parameter and Sand Grain Size Effect on Sediment Transport Over Vortex Ripples in the Orbital Regime. *Journal of Geophysical Research: Earth Surface* 124(1), 2–20.
- Finn, J. R., M. Li, and S. V. Apte (2016). Particle based modelling and simulation of natural sand dynamics in the wave bottom boundary layer. *Journal of Fluid Mechanics* 796, 340–385.
- Grant, W. D. and O. S. Madsen (1982). Movable bed roughness in unsteady oscillatory flow. *Journal of Geophysical Research* 87, 469–481.
- Harris, J. C. and S. T. Grilli (2014). Large eddy simulation of sediment transport over rippled beds. *Nonlinear Processes in Geophysics* 21, 1169–1184.
- Li, M. Z. and C. L. Amos (2001). Sedtrans96: the upgraded and better calibrated sediment-transport model for continental shelves .
- Liao, H. R. and H. S. Yu (2005). Morphology, hydrodynamics and sediment characteristics of the changyun sand ridge offshore western taiwan. *Terrestrial, Atmospheric and Oceanic Sciences* 16, 621–640.

Liao, H. R., H. S. Yu, and C. C. Su (2008, 2). Morphology and sedimentation of sand bodies in the tidal shelf sea of eastern taiwan strait. *Marine Geology* 248, 161–178.

Mellor, G. (2002). Oscillatory bottom boundary layers. *Journal of Physical Oceanography* 32(11), 3075 – 3088.

Nielsen, P. (1986). Suspended sediment concentrations under waves. *Coastal Engineering* 10(1), 23–31.

O'Donoghue, T., J. S. Doucette, J. J. van der Werf, and J. S. Ribberink (2006, 12). The dimensions of sand ripples in full-scale oscillatory flows. *Coastal Engineering* 53, 997–1012.

Richards, K. J. (1980). The formation of ripples and dunes on an erodible bed. *Journal of Fluid Mechanics* 99, 697–618.

Salimi-Tarazouj, A., T. J. Hsu, P. Traykovski, Z. Cheng, and J. Chauchat (2021). A Numerical Study of Onshore Ripple Migration Using a Eulerian Two-phase Model. *Journal of Geophysical Research: Oceans* 126(2), 1–27.

Schiller, L. and Z. Naumann (1935). A drag coefficient correlation. *Z. Ver. Dtsch. Ing.* 77(318), 318–320.

Sleath, J. (1982). The suspension of sand by waves. *Journal of Hydraulic Research* 20, 439–452.

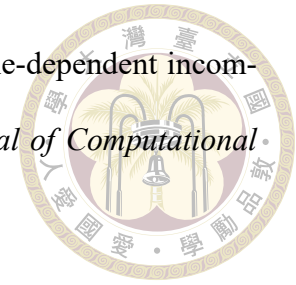
Soulsby, R. L. and J. S. Damgaard (2005). Bedload sediment transport in coastal waters. *Coastal Engineering* 52(8), 673–689.

Styles, R. and S. M. Glenn (2000). Modeling stratified wave and current bottom boundary



- layers on the continental shelf. *Journal of Geophysical Research: Oceans* 105(C10), 24119–24139.
- Tang, Y., E. A. J. F. Peter, J. A. M. Kuipers, S. H. L. Kriebitzsch, and M. A. van der Hoef (2014). A new drag correlation from fully resolved simulations of flow past monodisperse static arrays of spheres. *American Institute of Chemical Engineers AIChE J* 61, 688–698.
- Tenneti, S., R. Garg, and S. Subramaniam (2011, 11). Drag law for monodisperse gas-solid systems using particle-resolved direct numerical simulation of flow past fixed assemblies of spheres. *International Journal of Multiphase Flow* 37, 1072–1092.
- van der Werf, J. J., J. S. Doucette, T. O’Donoghue, and J. S. Ribberink (2007). Detailed measurements of velocities and suspended sand concentrations over full-scale ripples in regular oscillatory flow. *Journal of Geophysical Research: Earth Surface* 112(2), 1–18.
- van der Werf, J. J., V. Magar, J. Malarkey, K. Guizien, and T. O’Donoghue (2008). 2dv modelling of sediment transport processes over full-scale ripples in regular asymmetric oscillatory flow. *Continental Shelf Research* 28, 1040–1056.
- Van Rijn, L. (2007). Unified view of sediment transport by currents and waves. i: Initiation of motion, bed roughness, and bed-load transport. *Journal of Hydraulic Engineering* 133(6), 649–667.
- Warner, J. C., C. R. Sherwood, R. P. Signell, C. K. Harris, and H. G. Arango (2008). Development of a three-dimensional, regional, coupled wave, current, and sediment-transport model. *Computers and Geosciences* 34, 1284–1306.
- Yuan, J. and D. Wang (2019). An experimental investigation of acceleration-skewed oscillatory flow over vortex ripples. *Journal of Geophysical Research: Oceans* 124, 9620–9643.

Zang, Y. (1994). A non-staggered grid, fractional step method for time-dependent incompressible navier-stokes equations in curvilinear coordinates. *Journal of Computational Physics* 114(1), 18–33.



Zedler, E. A., R. L. Street, and M. Asce (2006). Sediment transport over ripples in oscillatory flow. *Journal of Hydraulic Engineering* 132(2), 180–193.

Zhou, J., Z. Wu, X. Jin, D. Zhao, Z. Cao, and W. Guan (2018, 12). Observations and analysis of giant sand wave fields on the taiwan banks, northern south china sea. *Marine Geology* 406, 132–141.